P-T path from garnet zoning in pelitic schist from NE Sardinia, Italy: further constraints on the metamorphic and tectonic evolution of the north Sardinia Variscan belt

Cruciani G.[1], Franceschelli M.[1*], Carosi R. [2], Montomoli C. [2]

[1]Dipartimento di Scienze Chimiche e Geologiche, Università degli Studi di Cagliari – S.S. 554 Cittadella Universitaria, 09042, Monserrato (CA), Italy

[2]Dipartimento di Scienze della Terra, Università degli Studi di Torino, Via Valperga Caluso 35, 10125 Torino, Italy

**Corresponding author:* francmar@unica.it

Abstract

Mylonitic micaschists in the south-eastern sector of the Posada-Asinara Shear Zone in the Axial Zone of the Sardinia Variscan chain were investigated for the reconstruction of their metamorphic evolution and P-T history. Micaschists underwent polyphase ductile deformation consisting of an old D1 deformation (~345–340 Ma) associated to shearing and folding and to a penetrative S1 axial plane foliation. The S1 foliation is progressively transposed by the D2 phase, which is associated with upright up to NE verging folds and dextral shear zones. Micaschists are characterized by abundant centimetric garnet crystals with strong compositional zoning. The garnet porphyroblasts (~15 vol%) are associated with plagioclase, quartz, biotite, staurolite, white mica, chloritoid and retrograde chlorite. Garnet presents an internal foliation identified by the iso-orientation of quartz inclusions sometimes arranged into a sigmoidal pattern suggesting rotation of the garnet during growth, discordant respect to the external S2 foliation. The S2 foliation is identified by the preferred orientation of micas and chlorite and by the alternance between quartzo-feldspathic and micaceous layers. The garnet core contains several small inclusions of quartz, rutile, apatite, and minor monazite and zircon. Additional inclusions, observed in the garnet domain around the core are ilmenite, chloritoid, staurolite and white mica. EMPA analyses reveal an even more complex chemical zoning consisting of garnet core, garnet mantle, and rim. The compositional isopleths that match the composition of the garnet core intersect with isopleths for the highest Si contents in K-white mica at about T 430–490 °C, P 1.3–1.4 GPa. Garnet rim isopleths and isopleths for the lowest Si contents in K-white mica indicate P-T conditions close to 560–630 °C/0.6–1.1 GPa. The resulting P-T path is clockwise, subdivided into two separate stages. The first stage is a prograde segment suggested by the garnet core to mantle compositional variation whereas the second reflects garnet rim growth during exhumation.

Keywords: microstructure; garnet; isochemical phase diagrams; P-T path; Variscan Sardinia

Introduction

Collision type orogens are characterized by polyphase deformation and metamorphism which help to unravel the tectonic and metamorphic evolution from the initial stages of collision up to the final ones often characterized by the extensional collapse of the belt when driving forces vanished. However the records of such a complex evolution are often scattered and both the tectonic structures and the metamorphic events are elusive especially for the initial stages, being overprinted by later deformation structures and associated metamorphism. In addition to this the development of new analytical techniques allows to go into further detail in the tectonic and metamorphic history as for example the use of petrochronology (Engi et al., 2017) which allows to link mineral ages to deformation and metamorphism (Williams and Jercinovic, 2012; Montomoli et al., 2013; Carosi et al., 2012). Among these techniques, the thermodynamic approach to the reconstruction of the rock history and evolution by means of isochemical phase diagrams (i.e. P-T pseudosection modelling) provides qualitative and quantitative information on the mineral assemblages that are stable at specific temperature and pressure. The obtained thermobarometric information is then interpreted to identify some specific tectonic setting and, eventually with the contribution of geochronology, its evolution in time. A few recent examples of this approach are given by, among the others, Cao et al. (2017), Thiessen et al. (2019), Liu and Massonne (2019), Massonne and Li (2020), Bovay et al. (2021), Freya George et al. (2021), Ganade et al. (2021). It is worth of note that garnet has often a dominant role, among the rock-forming minerals, for the accurate P-T conditions estimation in rock samples, being by far the key mineral to be investigated for rigorous reconstruction and better understanding of P-T evolution of basement areas and geological environments. Garnet is also known to be resilient to re-equilibration and, as a consequence, to be a good recorder of polymetamorphism (Thiessen et al., 2019 and references therein).

The Variscan belt of NE Sardinia has been regarded as a classical example of a well-preserved remnant of Variscan continental collision since long time, characterized by a Barrovian prograde metamorphism moving from SW to the NE from the biotite zone, through garnet zone, staurolite + biotite zone up to kyanite and sillimanite zone in the Posada Valley (see Fig. 1; Ricci et al., 2004). Detailed investigations in the chloritoid schists south from the Posada Valley allowed to define P-T conditions not compatible with previously detected low-grade metamorphic conditions (Cruciani et al., 2013). These authors found pressure values reaching c.a. 1.7 GPa that is significatively higher than the Barrovian pressure previously indicated for the garnet zone (c.a. 1.1 GPa; Cruciani et al., 2015a). Similarly, pressure values up to 1.4 GPa were found by Scodina et al. (2021) in the Posada

Valley amphibolites. This finding arises new problems and questions in the tectonic and metamorphic evolution of NE Sardinia metamorphic basement. The rocks recording HP conditions represent a slice of continental crust subsequently tectonically coupled with lower-grade metamorphics or do they represent the relict of the diffuse presence of HP in all the tectonic units? In the latter case, the Barrovian metamorphism occurred later than HP conditions?
To fix these questions, it is necessary to unravel the tectonic and metamorphic evolution of the Sardinian belt in the framework of the Southern Variscides.
With the aim to check if HP conditions were recorded elsewhere in the northern Sardinia basement, we investigated other selected micaschist samples characterized by a significant garnet compositional zoning cropping out in the southern side of the Posada Valley.

Geological setting and field geology

The Sardinia-Corsica block, being part together with the Maures-Tanneron Massif and Iberia peninsula of the Southern Variscan belt or Domain (Matte, 1986; Carmignani et al., 1994; Edel et al., 2018), is a transect of the Southern Variscan belt lacking Alpine overprint.
The metamorphic basement of Sardinia consists of metasedimentary and metaigneous rocks belonging to the northern margin of Gondwana, affected by Palaeozoic deformation and metamorphism resulting in a S- to SW-verging stacking of tectonic units with increasing metamorphic grade from SW to NE (Carmignani et al., 1994).
Along a south-west to north-east oriented profile, the Sardinia basement consists of the following three main tectono-metamorphic zones (Carmignani et al., 1994, 2001): External Zone, Nappe Zone (in turn subdivided into Internal and External Nappe) and Inner Zone (Fig. 1a).
The palaeozoic sequences of the External and Nappe Zones underwent metamorphic conditions varying from anchizone to greenschist facies conditions, with the only exception of the southernmost outcrops in the Capo Spartivento area (Mt. Settiballas Formation, in the External Zone) and Monte Grighini Unit (Nappe Zone) that reached amphibolite-facies metamorphic conditions (Cruciani et al., 2016; Cruciani et al., 2018, 2019).
Northwards to the Nappe Zone, the Inner Zone of the chain extends from northern Sardinia to southern and central Corsica (Massonne et al., 2018; Cruciani et al., 2021). In northern Sardinia, a regional scale transpressive shear zone known as the Posada-Asinara Shear Zone (PASZ), correlated to the Cavalaire Fault of the Maures–Tanneron massif and to the Ferriere –Mollieres Shear zone of the Argentera Massif of Western Alps (Schneider et al., 2014; Simonetti et al., 2020, 2021, 2018 and references therein), separates the Medium-Grade Metamorphic Complex (MGMC)

in the south from the High-Grade Metamorphic Complex (HGMC, also known as Migmatite Complex) in the north.

U–(Th)–Pb analyses on monazite from the PASZ indicate that the shear zone has been active at ~325–300 Ma in a transpressive tectonic setting, in agreement with the ages of the other dextral transpressive shear zones in the southern Variscan belt (Carosi and Palmeri, 2002; Carosi et al., 2020; Simonetti et al., 2018 2020). South of the PASZ, the MGMC mainly consists of micaschist and paragneiss with relics of HP assemblages (Cruciani et al., 2013) with sporadic quartzite, metabasite (Cruciani et al., 2010, 2015b) and orthogneiss (Helbing and Tiepolo, 2005).

The HGMC mainly consists of sedimentary-derived gneisses and HP migmatites (Massonne et al., 2013; Cruciani et al., 2014a,b; Fancello et al., 2018), migmatized orthogneiss, calc-silicate nodules, and metabasite lenses preserving eclogite and granulite facies relics (Cruciani et al., 2011, 2015a,b; Scodina et al., 2019, 2020, 2021). Layered amphibolites resembling leptyno-amphibolite complexes have also been described by Franceschelli et al. (2005).

In the eclogite, at Punta de li Tulchi (Fig. 1b), Palmeri et al. (2004) found U– Pb zircon weighted mean ages of 453 ± 14, 400 ± 10 and 327 ± 7 Ma, referred respectively to the protolith age, to the HP eclogitic event (or resulting from Pb loss during the main Variscan event), and to the retrogression to amphibolite facies P–T conditions. For one sample from eclogite from Punta de li Tulchi, a concordia age of 457 ± 2 Ma on magmatic zircons was interpreted as the minimum protolith age (Cortesogno et al., 2004). On a second group of zircons showing the complex zoning of HP metamorphic zircons, Cortesogno et al. (2004) obtained an age of 403 ± 4 Ma, interpreted as dating ‘‘the zircon crystallization during the high-grade event’’. This datum seems to confirm the value of 400 ± 10 Ma dubitatively proposed by Palmeri et al. (2004) as the actual age of the HP event in NE Sardinia.

Variscan tectono-metamorphic events in Corsica–Sardinia were accompanied by magmatic activity starting between 345 and 330 Ma with an earlier syn-tectonic Mg–K calc-alkaline association (Corsica), which was followed (310–280 Ma) by late- to post-tectonic high-K calcalkaline and late peraluminous granites (Rossi and Cocherie, 1991). The occurrence of polyphase ductile deformation in northern Sardinia is nowadays widely accepted and described by several authors (Carmignani et al., 1994; Connolly et al., 1994; Carosi and Palmeri, 2002; Carosi et al., 2005; Helbing et al., 2006; Elter et al., 2010; Graziani et al., 2020). The oldest deformation D1 (~345–340 Ma, Di Vincenzo et al., 2004; Carosi et al., 2012) is well preserved in some areas of the MGMC where it is associated to shearing and folding associated with a penetrative S1 axial plane foliation. Late D1 ductile/brittle shear zones, with top to the SW sense of movement, overprint the F1 folds. Towards north, the S1 foliation is progressively transposed by the D2 phase, which is associated with upright up to NE verging folds and dextral shear zones. The Variscan D2 transpressive shear is the main deformation observed in northern Sardinia (Carosi and Palmeri, 2002). Di Vincenzo et al. (2004) found ^{40}Ar–^{39}Ar ages of 320–305 Ma for most syn–D2 white mica in the MGMC, later confirmed by in-situ U-Th-Pb ages on zircon and monazite in the mylonitic rocks (Carosi et al., 2012, 2020). In the HGMC, two opposite senses of shear (top–to–the–NW and top–to–the–SE/NE) on the S2 foliation have been locally detected and interpreted by Elter et al. (2010) as being associated with the end of compression/crustal thickening (the first, top–to–the–NW) and with tectonic inversion during the exhumation of the metamorphic basement (top–to–the–SE/NE). A D3 deformation phase forming upright metric to decametric open folds developed subsequently. F3 folds are associated with an S3 axial plane crenulation cleavage. The D4 tectonic phase is revealed by metric to decametric folds with sub-horizontal axial planes (Cruciani et al., 2015c). An extended and detailed review of the Variscan orogeny in Sardinia can be found in Carmignani et al. (1994, 2001), Rossi et al. (2009), and Cruciani et al. (2015a).

The sampling area (Fig. 1, 40°36’17’’N, 9°35’29’’E) is located in NE Sardinia close to the boundary between the MGMC and the HGMC, in the south-eastern sector of the PASZ. The Variscan metamorphic rocks cropping out in this area, which belongs to the staurolite + biotite zone of the Barrovian Sardinian metamorphic sequence, mainly consist of micaschist and paragneiss with an increasing metamorphic grade from south to north. Granodioritic orthogneiss and augen gneiss, being part of the so called Lodé-Mamone antiform, crop out in the southern sector of the investigated area, whereas amphibolite lenses, embedded within the metasedimentary sequence of the kyanite + biotite zone, are aligned along the PASZ a few kilometers north from the study area.

At least twenty metapelitic rock samples were collected along a road cut in the forest, near to a restored traditional small building locally known as “Su Pinnettu” (Fig. 1) a few km north of the SP50 road connecting S. Anna (at east) and Lodè (at west) villages. The outcrop, a few tens of meters in width and in part covered with bushes and vegetation, consists of silver-coloured mylonitic micaschists characterized by the occurrence of abundant garnet crystals visible by naked eyes (Fig. 2a,b). The garnet crystals, which are nearly idiomorphic, appear to be homogeneously distributed in the rock matrix. For a detailed structural reconstruction of the geometrical relationships between the metasedimentary sequences, granodioritic orthogneiss and augen gneiss exposed in the study area the reader is referred to Carosi et al. (2005, 2020).

Methods

All collected samples were prepared in thin section for petrographic and microstructural investigation. Among these, two samples (FZ13 and FD3X) were selected for thermodynamic modelling based on their spectacular texture and garnet chemical zoning. Sample FZ13 was also analyzed for rutile thermometry and monazite dating by EMP.

Microstructural investigations and BSE imaging on the corresponding polished and carbon-coated thin-sections were obtained with a FEI Quanta 200 SEM equipped with a nitrogen-free Thermofisher™ UltraDry EDS Detector at CeSAR, Centro Servizi d'Ateneo per la Ricerca, Università di Cagliari. Chemical analyses of silicate minerals were performed with a CAMECA SX100 electron microprobe (EMP) with five wavelength-dispersive spectrometers installed at the Institut für Anorganische Chemie, Universität Stuttgart. The conditions for the silicate mineral analyses, including the analytical errors, were reported by Massonne (2012). X-ray concentration maps for garnet were prepared by stepwise movement of a thin section under the electron beam of the EMP by using counting times per step of 100 ms and an electric current of 50 nA. Zirconium in rutile was analysed by the EMP with 15 kV, 200 nA and 5 μm spot size using a TAP crystal and counting times on peak and background of 200 s each according to the method described in Li et al. (2017). For in situ dating of monazite with the EMP (Cocherie and Albarede, 2001), a focussed beam was used with 150 nA beam current, and 20 kV acceleration voltage. The detailed analytical procedure is fully described in Massonne et al. (2018). Estimation of the garnet core (and garnet mantle) volume respect to the corresponding garnet crystal was obtained from the EMP X-ray maps by the free image-analyses software Scion Image.

Mineral structural formulae and mineral molar fractions of the solid-solution components were calculated with CALCMIN (Brandelik, 2009). Determination of modal contents from X-ray maps were performed with the public domain image processing and analysis software Scion Image (version Beta 4.0.2).

P-T pseudosections were calculated in the system SiO_2–TiO_2–Al_2O_3–FeO–MgO–CaO–MnO–Na_2O–K_2O with the internally consistent thermodynamic dataset of Holland and Powell (1998), upgraded in 2011, using the 2019 version of Perple_X software package (Connolly, 2009). Isomodes and compositional isopleths were calculated by Werami. All Fe was assumed to be Fe^{2+}, because Fe^{3+}-bearing oxides are absent in the studied samples and the Fe^{3+} contents in the main minerals (garnet, chlorite, chloritoid, white mica) are negligible. The calculation was done in the P-T range of 0.3–2.1 GPa and 400–650 °C with water in excess. Solution models used in the P-T pseudosection calculation were those of White et al. (2014) for garnet, biotite, white mica, staurolite, chloritoid, ilmenite and Benisek et al. (2010a,b) for plagioclase feldspar. For cordierite the ideal solid-solution model hCrd was used whereas the model by Holland et al. (1998) for chlorite was used in order to obtain P–T stability fields comparable to those by Gaidies et al. (2008), mainly in the low P–T boundary of the garnet-forming reaction.

Petrography

The studied micaschist sample is a silver-coloured strongly foliated rock with mylonitic fabric characterized by the occurrence of reddish to brownish garnet poikiloblasts up to 1 cm in size and yellowish staurolite porphyroblasts (Fig. 2b). At the micro scale, a centimeter-thick alternation of light-coloured, quartzo-feldspathic layers with darker layers rich in mica and mafic minerals is observed (Fig. 2b). Centimetric garnet and staurolite porphyroblasts (Fig. 3a,b,c) and plagioclase crystals (Fig. 3d) are enveloped by the main S2 schistosity which is mainly identified by the orientation of white mica and chlorite in phyllosilicate-rich layers and by the compositional alternance between quartzo-feldspathic and micaceous layers. Although the size, distribution, and modal abundance of garnet, micas and staurolite are strongly variable among the different samples and even among the different layers and/or microdomains of the same sample, the microscopic investigation on thin sections of about one dozen samples reveals that the schist is mainly composed (on average) of plagioclase (10 vol%), quartz (25 vol%), garnet (15 vol%), biotite (10 vol%), staurolite (up to a maximum of 10 vol%), muscovite (30 vol.%), chloritoid and chlorite. Ilmenite, rutile, corundum, zircon, monazite, paragonite, margarite, apatite and tourmaline occur as accessory phases in the rock matrix and/or as inclusions inside the above mentioned porphyroblasts.

Within the rock matrix a faint S1 foliation is sometimes preserved by the elongation of micas and chlorite in mica-rich microlithons. Inside the garnet porphyroblasts, straight to gently curved, pre-D2 relict foliation(s) is identified by the iso-orientation of several submicroscopic quartz microinclusions sometimes arranged into a sigmoidal pattern suggesting rotation of the porphyroblast during its growth (see Fig. 3a,e). Poorly-defined pre-D2 relic foliation is finally identified by a very weak iso-orientation of muscovite flakes inside plagioclase crystals (see dotted line in Fig. 3d). The garnet porphyroblasts are rounded or, less frequently, slightly elongated (Fig. 3a,e,f). The garnet core domain contains several small inclusions of quartz, rutile, apatite, sporadic monazite and zircon, and trace amounts of chlorite. As already mentioned, these inclusions are arranged as curved inclusion trails often following an oriented spiral-shaped and/or sigmoidal arrangement (snowball garnet) and recording an earlier S1 schistosity preserved inside the garnet (Fig. 3e). Rutile inclusions in the garnet core are sporadically associated to (and/or partially replaced by) ilmenite. Rutile replacement by ilmenite is observed also in the rock matrix. Additional inclusions, that were observed only in the garnet rim domain, are ilmenite and chloritoid (Fig. 3f,g), and subordinate staurolite and muscovite. Worthy of note, is the absence of rutile inclusions outside from the garnet core. The few quartz inclusions observed in the rim domain are significantly bigger than the several ones that are found in the garnet core (Fig. 3f). Garnet porphyroblasts are often flanked by strain shadows filled with medium-grained quartz and chlorite or with a fine-grained intergrowth of quartz, phyllosilicates (muscovite and chlorite) and opaques. The staurolite porphyroblasts (up to 0.5cm in length) contain rounded quartz inclusions, euhedral tourmaline inclusions, elongated and oriented ilmenite microcrystals and very small, subordinate monazite and zircon (Fig. 3h). In some samples, several small garnets up to 0.4-0.5mm in size are included in staurolite. These porphyroblasts appear strongly fractured, surrounded by chlorite and/or characterized by chlorite overgrowth along veins and fractures. Similarly to what observed for garnet, the staurolite porphyroblasts are also bordered by strain shadows filled by chlorite, white mica and/or quartz.

Chloritoid, which can be sporadically associated with paragonite, margarite or corundum trace amounts (Fig. 3g), was only found as inclusions (<1mm in length) in garnet. Corundum, in the aforementioned occurrence, can be observed at the chloritoid/garnet interface.

Muscovite is the main constituent, together with chlorite and biotite (in order of decreasing abundance) of the phyllosilicate-rich rock portion. An earlier generation of potassic white mica was also found as small inclusions armoured inside garnet and plagioclase, whereas paragonite was only observed growing at the expense of chloritoid in garnet.

Tourmaline, which mostly occurs in single crystals up to half a millimeter in size is compositionally zoned and contains very small monazite, quartz and ilmenite microinclusions.

The mineral assemblage and metamorphic evolution scheme based on the microstructural relationships above described, with special reference to garnet and staurolite porphyroblasts, their mineral inclusions, and surrounding S2 matrix, are summarized in Fig. 4.

Mineral chemistry

Representative microprobe analyses of garnet and staurolite porphyroblasts, together with analyses of matrix feldspar, biotite, white mica, chlorite, and inclusions of chloritoid and ilmenite from two selected samples of the micaschist from the southern side of the PASZ are given in Table 1.

Mg, Ca, Mn, Fe and Y compositional X–ray maps of two selected garnet porphyroblasts from the two samples are shown in Figs. 5 and S1 of Supplementary Material, respectively, whereas core–rim compositional profiles across the garnets in terms of molar fractions of grossular, pyrope, almandine and spessartine components are reported in Fig. 6. The EMP X–ray mapping and rim–core–rim garnet compositional profiles reveal a well-defined zoning of the garnet components characterized by four compositional domains (core, mantle, rim, outer rim).

The composition of the large garnets core is Ca- and Mn-rich ($Alm_{45–50}Grs_{21–27}$ $Prp_{<2}Sps_{25–30}$) and differ significantly from the iron-rich compositions of the surrounding shells. A significant decrease in grossular and spessartine contents are observed towards the mantle ($Alm_{60-80}Grs_{10–20}Prp_{2–5}Sps_{10-20}$). The inner and outer rim are $Alm_{80-85}Grs_{6–10}Prp_{5–7}Sps_{1-5}$ and $Alm_{>85}Grs_{<5}Prp_{>8}Sps_{<1}$, respectively. Additionally, a systematic decrease of titanium content has been observed from garnet core (TiO_2 0.1-0.2 wt.%) to rim (0.04–0.08 wt.%). X-Ray mapping of Yttrium (Fig. S1) shows a discontinuity of this element corresponding to the mantle/rim interface of the garnet.

Staurolite porphyroblasts show a very slight compositional zoning. They show X_{Mg} ratio of 0.14–0.13 in the core and 0.11–0.10 in the rim. Ti and Mn contents in staurolite is ~ 0.1 and 0.02–0.05 apfu, respectively. Staurolite porphyroblasts and staurolite inclusions in garnet rim show the same composition. Chloritoid shows X_{Mg} ratio of 0.12–0.13. The isolated plagioclase single crystals found in the rock matrix are unzoned oligoclase, with their composition mostly in the range Ab: 80–90 mol.%. Biotite in the matrix has X_{Mg} ratio of 0.44–0.46, similar to X_{Mg} ratio in matrix chlorite which is ~ 0.4. Chlorite growing on veins and fractures of staurolite shows similar X_{Mg} value (0.4).

K-white mica was analyzed in garnet inclusions and in the rock matrix, the latter being aligned to the S2 schistosity. Considering all mica analyses, a wide range of variability for Si from 6.10 to 6.38 apfu (Fig. 7) was observed, with Fe^{2+}, Mg, and Na contents in the ranges 0.08–0.23, 0.05–0.22 and 0.1–0.8 apfu, respectively. A slight increase of Fe, Mg, and significant decrease of Na is observed with rising Si content (Fig. 7). A more restricted range of compositions was observed in muscovite inside the garnet porphyroblasts which are on average, characterized by highest Si, Mg, Fe and lowest Na contents (Si 6.3–6.38, Fe 0.17–0.27, Mg 0.05–0.15, Na 0.09–0.25 apfu) as compared to muscovite from the rock matrix (compare full and empty symbols in Fig. 7).

Muscovite in garnet has X_{Mg} 0.31–0.38 whereas muscovite from matrix has X_{Mg} 0.41–0.44 (Table 1).

Paragonite shows X_{Mg} close to 0.15 and Na of about 1 apfu. Ilmenite enclosed in staurolite shows lower MnO content (< 1.5 wt.%) as compared to ilmenite from the matrix which usually contains more than 2.0 wt.% MnO. Ilmenite inclusions in garnet show decreasing manganese content from core (Mn 0.06 apfu) to rim (0.02) of the garnet.

Compositionally zoned tourmaline crystals (up to 500–600 µm in size) show a systematic decrease of iron counterbalanced by increasing magnesium from their core to the rim. The tourmaline rim generally does not exceed 200 µm in thickness.

Pressure and temperature evolution

The P–T pseudosection for sample FZ13 shown in Fig. 8a is dominated by quadri- and tri-variant fields with pentavariant fields mostly confined at HP–HT conditions and some minor divariant fields at low T- high P conditions. Two white mica (potassic and sodic) occur almost in the entire investigated P–T range, with the exception of potassic white mica that disappears in correspondence of the biotite entry. Garnet, probably overstabilized by the MnO component, is present in the mineral assemblage of almost all the multivariant fields modelled by the calculation, with the exception of the small P–T fields at the lower left corner of the P-T pseudosection. Lawsonite is modelled at T<500 °C and P >1.1 GPa, whereas chloritoid is predicted in the middle, upper part of the equilibrium assemblage diagram, mostly together with chlorite and/or lawsonite. Biotite occurs at T > 550 °C and P < 1 GPa. Albite/plagioclase (depending on temperature) are stable at P not higher than 0.8 GPa. The compositional isopleths for garnet and white mica calculated with Werami are given in Fig. 8b-f. A second P–T pseudosection calculated for micaschist sample FD3X, and the corresponding compositional isopleths for garnet and white mica are shown in Fig. S2 of Supplementary Material. Boundaries of the stability P-T fields for the most relevant mineral phases (garnet, chloritoid, lawsonite, staurolite, biotite, rutile, ilmenite) and compositional isopleths for X_{Mg} ratio in chloritoid are shown, for both the above mentioned samples, in Fig. S3 of Supplementary Material.

Rutile thermometry

Chemical analyses of oxides (including ZrO_2) were determined by EMP on in-situ rutile grains on the petrographic thin section of the selected micaschist sample FZ13. This analytical strategy allowed us to discriminate directly during the analytical run rutile in the rock matrix from rutile included in the core domain of the garnet. Rutiles preserved in the core domain of the garnet have detectable ZrO_2 concentrations suitable for temperature estimates.

The temperatures estimated from the Zr-in-rutile thermometer applied to thirtyfive analyses of rutile grains included in the cores of garnet crystals from sample FZ13 are reported in Table S1 of the Supplementary Material together with the ZrO_2 concentrations of each single analytical spot. The pressure that was considered for the calculation of the calibration by Tomkins et al. (2007) was 0.9 GPa. This calibration in fact considers, unlike those by Watson et al. (2006) and Zack et al. (2004), a slight pressure dependence of the thermometer.

The rutile temperatures estimated for 0.9 GPa by the Tomkins et al. (2007) calibration in sample FZ13 are in the 528–614 °C range with an average value of 577 °C, whereas those estimated with the Kohn (2020) calibration yielded a slightly lower temperature range of 478–573 °C (average: 531 °C) (Table S1 and histograms in Fig. S4 of Supplementary Material). The estimated error is ~30 °C (Tomkins et al., 2007) and minimum uncertainty ±25 °C (Kohn, 2020). The other two, not pressure-dependent, calibrations of the Zr-in-rutile thermometer gave: 498–665 °C, average: 594 °C

(Zack et al., 2004) and 520–609 °C, average: 570 °C (Ferry and Watson, 2007). The rutile grains from the rock matrix yielded ZrO_2 concentration below detection limit.

Calculation results and P–T path

For the P–T path reconstruction we considered the zoned garnet composition from core to rim. The whole-rock composition, obtained by XRF analyses and corrected for apatite, was used to calculate the P-T pseudosections in order to decipher the P-T conditions of garnet core formation (Table 2). For the growth of garnet rim, an effective bulk composition (EBC1, Table 2) was obtained by subtracting garnet core + mantle composition after determining the garnet mode in the rock (15%) and the volume of garnet core (30%) + mantle (40%) with respect to the total garnet. The P–T pseudosections shown in Figs. 8, S2 were contoured with Werami by isopleths for molar fractions of garnet components (Ca, Fe, Mn; see Fig. 8b-d) and modal contents of garnet (in vol.%, Fig. 8e).

The metamorphic assemblage preserved in the garnet core of the studied schists (garnet + muscovite + quartz + rutile) does not allow to constrain a sufficiently narrow area in the P–T pseudosection. However, the garnet isopleths representing the composition of garnet core (i.e. the composition with the highest Mn considered to be the earliest grown garnet: $Grs_{0.26}Alm_{0.45}Sps_{0.28}$ in garnet from sample FZ13, see Table 1) intersect in the field Grt + Ms + Pg + Cld + Chl + Lws + Qz + Rt indicating P–T conditions in the range 430–480 °C/1.4 GPa in sample FZ13 (Fig. 9a) and suggest similar P–T conditions in sample FD3X (Fig. 9c). The garnet isopleths are intersected by those representing the highest Si contents in K-white mica included in garnet (6.30–6.38 apfu, see Table 1), at 1.5/1.7 GPa (sample FZ13, Fig. 9a) and 1.5 GPa (sample FD3X, Fig. 9c). P–T pseudosection modeling predicts lawsonite content lower than 2.5 vol.% (in modal amount) and chloritoid not higher than 10 vol.% at the above mentioned P–T conditions.

The grossular and spessartine components of garnet in the studied samples progressively decrease, whereas the almandine and pyrope components increase from the garnet core to the outer rim (see Table 1 and Fig. 5). This compositional zoning was already observed in similar rock samples from the garnet-zone of NE Sardinia investigated by Cruciani et al. (2013). According to the garnet compositional isopleths shown in Figs. 8, S2, the decrease in spessartine and increase in almandine components point to an increase of temperature from the core to the rim of the garnet. Following the same approach, but using the above mentioned fractionated effective bulk composition (Table 2), the rim composition of the same garnet was used to define the P–T conditions of rim formation. Garnet isopleths representing the composition of garnet rim ($Grs_{0.02}Alm_{0.85}Sps_{0.01}Prp_{0.12}$) intersect with the isopleths representing the lowest Si contents in K-white mica from matrix (6.1 apfu, Table

1) and with the X_{Mg} of staurolite (0.14) in the field Grt + Ms + Pg + St + Chl + Rt/Ilm, suggesting P–T conditions in the range 560–620 °C/0.65–1.1 GPa in sample FZ13 (Fig. 9a) and 590–630 °C/0.7–1.05 GPa in sample FD3X (Fig. 9c) for the outer rim of garnet.

The approach explained above allowed us to define two ellipses representing P–T conditions for garnet core and garnet rim formation, respectively, for the two investigated samples (Fig. 9a,c). However, the strong garnet zoning revealed by the X-ray maps shown in Fig. 5, provides the possibility to reconstruct and draw a more complete P-T path by using the Compositional Zoning in Garnet and its Modification by diffusion (CZGM) software by Faryad and Ježek (2019). This software allows to compare the initial profiles of the garnet components, along any P-T trajectory that can be drawn in the P-T space of interest, with the observed garnet profiles measured by the EMP (Faryad and Ježek, 2019; Kulhánek et al., 2021). For this purpose in Matlab (version R2020b) the *make_path* function of CZGM was used to draw in the P-T space 400-650 °C/0.3-2.1 GPa the modelled P-T trajectories that give the best fit with the measured garnet profiles, considering the profile of each garnet component (X_{Fe}, X_{Mg}, X_{Ca} and X_{Mn} in Fig. 9b,d). To define the position, where garnet started to grow along the selected PT path garnet_no=30 was selected when running the *make_garnet* CZGM function. A good fit between the measured and initial garnet profiles is obtained only modeling two different stages of the P-T path for the core and rim profiles, separately. The garnet core + mantle prograde growth occurred along stage (a) of the P-T path shown in Fig. 9 whereas the rim growth occurred mainly along stage (b), which was calculated after fractionation of the core + mantle (bulk minus core & mantle in Table 2). The comparison between the calculated initial profiles along P-T path stages (a) and (b) with the profile measured in the garnet core and mantle and with that of garnet rim, respectively, are given in Fig. 10a,b and c,d. The fit is fairly good in terms of concentrations and trend of the garnet components, in particular for the inner part of the garnet. Slightly lower almandine content in the initial profile respect to the measured spots in garnet rim could be tentatively related to the entry of staurolite or to the breakdown of chloritoid coeval with rim growth.

At the end of the P-T path, approximately below 1 GPa, the P–T path becomes tangential to the garnet isomodes, implying that new garnet cannot form. The two separate stages of the P-T path imply that the external part of the garnet core possibly underwent partial resorption (dashed line in Fig. 9) at the onset of exhumation, as described by Faryad et al. (2019) for garnets from Papua New Guinea.

In summary, the grossular decrease and almandine increase from garnet core (Grs ~25; Alm ~ 50) to mantle (Grs ~15; Alm > 60) is compatible with a prograde segment of the P-T path from garnet core formation at 430–490 °C/1.4 GPa to pressure peak at 1.7 GPa. The subsequent, even stronger, increase in almandine (Alm > 80) and abrupt decrease in spessartine (~ 1) and grossular (< 5) in the rim fit with temperature increase, accompanied by pressure decrease, up to the metamorphic peak in the staurolite + biotite field close to 600 °C. The resulting P-T path is clockwise with peak pressure diachronous with respect to the peak of metamorphism.

Dating results of monazite

Monazite was analyzed in micaschist sample FZ13, where nineteen grains, ten from the rock matrix and nine preserved as inclusions in garnet rim, staurolite, and tourmaline, were analyzed directly on thin sections (Table 3). Monazites are small, rounded and/or anhedral grains with maximum size of 50–60 µm. The analyzed monazite systematically contains low Y_2O_3 (0.01 to 0.30 wt.%), which is by far lower than the 2 wt.% Y_2O_3 content indicated by Massonne et al. (2018) for monazite that formed before garnet. Additionally, compositional X-ray maps, show that, at least in a few selected monazite grains in the matrix, the U and Th content increases from the centre to the periphery of the crystals, so that a discontinuous, and very thin, U- and Th-enriched rim that surrounds a more wide homogeneous nucleus can be observed. However, the thickness of the discontinuous rim (only a very few microns in size) is not enough to be analyzed. For this reason, in all monazite grains, including those with the discontinuous rim, we analyzed by a single spot size the middle, homogeneous nucleus of the monazite. The monazite age results are reported in Table 3 and are plotted versus the different textural position of the analyzed grains in Fig. S5 of Supplementary Material.

The monazite in situ dating yielded ages comprised between 417 and 322 Ma (average 377 Ma) for monazite inclusions in garnet rim, staurolite, tourmaline and 402–330 Ma (average 357 Ma) for monazite in the rock matrix.

The older analyzed monazite grains correspond to small crystals included inside the garnet or in tourmaline. The monazite in garnet aged 346 Ma (grain n. 10 in Table 3), i.e. younger than the other included monazites, probably suffered from its textural position, which were in proximity of a garnet fracture.

The six grains that yielded an age older than 390 Ma are characterized by Th/U ratio < 8, with four grains out of these six with Th/U lower than 6. Their Y_2O_3 content is comprised between 0.04 and 0.15 wt.%. The younger monazite ages correspond to grains from the rock matrix, with the only exception of grain n. 8 aged 402 Ma (Table 3), which possibly reflects an inherited old monazite portion. The two younger grains (330 and 322 Ma), which correspond to monazite in the rock matrix, yielded higher Th/U ratios of 8.1 and 8.8, and Y_2O_3 0.16 and 0.15 wt.%, respectively. All the remaining monazite grains, with ages comprised between 388–346 Ma, show Th/U ratios in the

5-12 range. 1σ age error for monazite from the matrix is mostly comprised between 16 and 20, and, on average, slightly higher (17–28) for monazite included in other mineral phases.

Discussion

The clockwise P-T path obtained in this paper consists of a prograde segment which, after the peak pressure is followed by an increase in temperature of about 100 °C (from 500 to 600 °C) up to the peak metamorphism in the staurolite field. The temperature increase is accompanied by a significant pressure decrease of at least 1.0 GPa (from 1.7 to 0.7 GPa). P–T paths with diachronous pressure and temperature peaks were already known in the Variscan chain of Sardinia since Franceschelli et al. (1989). Although the areal extent of HP metamorphism in Sardinia has to be further investigated, this P-T trajectory is compatible with an HP stage, eventually in a subduction regime, of the studied mylonitic schist before the Barrovian-type metamorphism.

On the basis of the new data the following schematic tectono-metamorphic history can be proposed:
- convergence between Gondwana and Armorica and subduction of the oceanic lithosphere below Armorica continent. In this stage oceanic lithosphere recorded conditions of HP–LT (e.g. P 0.9-1.4 GPa and T 530–590 °C in the boudins of metabasites in the Posada Valley shown in Fig. 1; Scodina et al., 2021) (yellow asterisk in Fig. 11a);
- collision and HP–LT metamorphic conditions recorded in the more distal part of the continental lithosphere (pressure peak at 1.7–1.8 GPa) probably coeval with the development of D1 deformation (red asterisk in Fig. 11b). At the same time metamorphosed oceanic crust is exhumed during D1 deformation event and thrusted above the subducting continental crust. In this way we can explain the occurrence of boudins of metabasites recording similar peak P values of the hosting rocks in the Posada Valley. The suture rocks are tectonically dismembered and transported far to the South (Schneider et al., 2014) and deformed by the following deformation events.
Late D1 exhumation of the HGMC starts by activation of NW–SE striking and top–to–the N–NW sinistral shear zones with a major dip-slip component of movement (PASZ in northern-central Sardinia; Frassi et al., 2009; Carosi et al., 2012). This caused the tectonic repetition of the metamorphic sequence and the building up of the nappe pile by oblique thrusting of the HGMC onto the L-MGMC;
- after the pressure peak, regional Barrovian metamorphism in an exhumation setting (Carosi and Palmeri, 2002; Cruciani et al., 2013) led to porphyroblast growth (garnet rim, staurolite) with T increasing towards the NE (Franceschelli et al., 1989; Ricci et al., 2004) up to peak metamorphism (570 °C/0.8-0.9 GPa) in a transpressional regime during the development of the D2 event. A

possible reason for heating after the peak pressure (Cruciani et al., 2015a,b) could be the thermal flow related to slab break-off (Faryad and Cuthbert, 2020) also responsible for the production of Mg–K igneous suite, as in the Bohemian Massif and in Corsica (Janoušek and Holub, 2007; Casini et al., 2013).

- the peak metamorphism was followed by a mylonitic deformation which occurred along the PASZ which was active at ~325–300 Ma in a dextral, transpressive setting. The new monazite ages in the studied micaschist span between c.a. 420 and 320 Ma with a mean error around 21 Ma. The error is quite high and do not allow to precisely discriminate the tectonic events. However making a comparison with *in-situ* U-Th-Pb analyses of monazite in the same area by Carosi et al. (2020) we can better link the new P-T-t path and the tectonic setting.

Older ages, between 330 and 390 Ma, broadly fall within the expected age of the D1 deformation event characterized by increasing P and T (Di Vincenzo et al., 2004; Carosi et al., 2012). An age close to HP metamorphism in the metapelite may be constrained by the Ar/Ar age of ~340 Ma on phengitic white micas along the S1 foliation within albite porphyroblasts a dozen km south of the study outcrops (Di Vincenzo et al., 2004). The Ar/Ar age of ~340 Ma is in agreement with the timing of maximum thickening in the Internal Nappes and may approximate the white mica crystallization age during the D1 phase. However, it is possible that the phengitic white micas, partially re-equilibrated at upper crustal levels, do not represent the actual age of the HP metamorphism and could be a lower limit of the HP event. In this framework ages from 340/350 to 390 could be broadly attributed to HP event. However, a reasonable lower limit of deformation and metamorphism is constrained by the occurrence of Middle Devonian conodonts in the marbles of the northernmost part of the Internal Nappes (Di Vincenzo et al., 2004). Older ages up to 420 Ma can be interpreted as inherited ages.

Younger monazite ages around 330 and 320 Ma, detected in the rock matrix, are characterized by a slight increase of Y with respect to older monazite ages. This is in full agreement with the U/Pb and U/Th ages of 330–315 Ma of monazite from samples very close to the study ones, where the structural position of the grains (within staurolite rims and along the S2 mylonitic foliation) and the chemical composition of the dated domains showing high-Y rims, allow to attribute these ages to dextral transpressional shearing (Carosi et al., 2020). Comparable ages detected in monazite rims characterized by high Y and low Th content were attributed to the exhumation of the mylonitic rocks by dextral transpression along the PASZ (Carosi et al., 2012, 2020).

Transpressional deformation continued at upper crustal levels with decreasing temperature, starting from the amphibolite-facies (D2) down to the greenschist-facies (D3) as testified by syn-kinematic chlorite along S3 foliation and incipient subgrain rotation recrystallization superimposed to grain

boundary migration in quartz (Graziani et al., 2020). Microstructural data showed an evolution of the D2-D3 transpressional deformation from a pure shear towards a simple shear dominated transpression (Carosi et al., 2020; Graziani et al., 2020) in the time span 330/325 – 300 Ma.
Our new data confirm that rocks affected by the PASZ underwent HP during the D1 collisional stage, as was already observed in HP micaschist and paragneiss cropping out near to Punta Gurturgius (see Fig. 1), ca. 10 km south from the studied area (Cruciani et al., 2013). The new calculated pressure values obtained in this paper pointed to 0.6 GPa higher values with respect to the pressure estimations up to now calculated in the literature for the PASZ (maximum P c.a. 1.1 GPa, Carosi et al., 2020), implying a different shape and meaning of the P-T-t path. In the studied samples staurolite stability field is not reached during increasing P and T but during decompression and heating. Maximum P was reached during D1 collisional stage during the subduction of the continental crust. On the other hand staurolite grew after D1 deformation phase and mostly from pre- to syn-D2 dextral transpressional event along with syn-kinematic biotite and white mica (Carosi and Palmeri, 2002; Carosi et al., 2020). This marks an important link between P-T-t and D2 dextral transpression allowing us to date this part of the P–T–t path at 325-300 Ma. Dextral transpression started after 330 Ma marked by the growth of staurolite during decompression from nearly 0.9 GPa. The first part of the exhumation (nearly 0.8 GPa) should be acquired before dextral transpression possibly by top–to–the SW shear zones with a dip-slip kinematics as highlighted in central-northern Sardinia where older down-dip shear zones were overprinted by younger dextral shear zones with a major strike-slip movement closely related to the PASZ (Carosi et al., 2009; Frassi et al., 2009). Steeply dipping top–to–the–S and SW shear zone should be efficient to quickly exhume HP rocks.
The observation that the pressure values recorded by the HP event decrease from north to south of the island suggests that continental crust slices were differently involved by the subduction during the orogenetic event. In this framework we confirm that Barrovian-type metamorphism cannot be longer regarded as the main prograde metamorphism affecting NE Sardinia (Cruciani et al., 2013a). The occurrence of HP metamorphism in the studied metapelites in the PASZ suggests that the occurrence of HP rocks is not sporadic or limited to small slices or boudins of continental crust but possibly affected all the MGMC up to now regarded as a classical example of prograde Barrovian metamorphism in Sardinia.

Concluding remarks

The studied micaschist samples allowed to shed some light on the following points:

- the garnet core composition together with the occurrence of chloritoid and high Si-muscovite in garnet reveal high – pressure conditions pre-dating the Barrovian metamorphism.
- the clockwise P-T path shows a prograde segment reaching peak pressure at about 1.7GPa. The temperature peak is reached later at about 600 °C, in the staurolite stability field. The P-T path is subdivided into two separate stages. The first stage records garnet core to mantle chemical zoning whereas the second reflects garnet rim growth.
- The new monazite ages in the studied micaschist span between c.a. 420 and 320 Ma with a mean error around 21 Ma. HP metamorphism should be bracketed between 340/350-390, whereas older ages up to 420 Ma can be interpreted as inherited ages. Younger monazite ages around 330 and 320 Ma, in the rock matrix, are attributed to dextral transpressional shearing.
- The systematic finding of new HP rocks in northern Sardinia suggests that the Variscan belt setting is probably more complex than the simple prograde Barrovian sequence described so far.

Acknowledgements

Thomas Theye (Stuttgart) is acknowledged for the support of our work with the electron microprobe. Financial support was provided by Regione Autonoma della Sardegna, L.R. 7/2007, research programme "Il blocco Sardo–Corso: area chiave per la ricostruzione della geodinamica varisica" CUP J81G17000110002. The authors appreciate the comments and suggestions by A. Langone (CNR–IGG Pavia) and one anonymous reviewer that helped to improve the manuscript.

References

Benisek, A., Dachs, E., Kroll, H., 2010a. A ternary feldspar-mixing model based on calorimetric data: development and application. Contrib. Mineral. Petrol. 160, 327–337.

Benisek, A., Dachs, E., Kroll, H., 2010b. Excess heat capacity and entropy of mixing in ternary series of high-structural-state feldspars. Eur. J. Mineral. 22 (3), 403–410.

Bovay, T., Lanari, P., Rubatto, D., Smit, M., Piccoli, F., 2021. Pressure–temperature–time evolution of subducted crust revealed by complex garnet zoning (Theodul Glacier Unit, Switzerland). J. metamorphic Geol. 40, 175–206.

Brandelik, A., 2009. CALCMIN – an EXCEL^{TM} Visual Basic application for calculating mineral structural formulae from electron microprobe analyses. Comput. Geosci. 35, 1540–1551.

Cao, D.D., Cheng, H., Zhang, L., 2017. Pseudosection modelling and garnet Lu–Hf geochronology of HP amphibole schists constrain the closure of an ocean basin between the northern and southern Lhasa blocks, central Tibet. J. metamorphic Geol. 35, 777–803.

Carmignani, L., Carosi, R., Di Pisa, A., Gattiglio, M., Musumeci, G., Oggiano, G., Pertusati, P.C., 1994. The Hercynian chain in Sardinia (Italy). Geodin. Acta 7, 31–47.

Carmignani, L., Oggiano, G., Barca, S., Conti, P., Eltrudis, A., Funedda, A., Pasci, S., Salvadori, I., 2001. Geologia della Sardegna (Note illustrative della Carta Geologica della Sardegna in scala 1:200000). Memorie descrittive della Carta Geologica d'Italia, Vol. LX, Servizio Geologico Nazionale. Istituto Poligrafico e Zecca dello Stato, Roma, 283 pp.

Carosi, R., Palmeri, R., 2002. Orogen-parallel tectonic transport in the Variscan belt of northeastern Sardinia (Italy): implications for the exhumation of medium-pressure metamorphic rocks. Geol. Mag. 139, 497–511.

Carosi, R., Frassi, C., Iacopini, D., Montomoli, C., 2005. Post-collisional transpressive tectonic in northern Sardinia (Italy). J. Virtual Explor. 19.

Carosi, R., Petroccia, A., Iaccarino, S., Simonetti, M., Langone, A., Montomoli, C., 2020. kinematics and timing constraints in a transpressive tectonic regime: the example of the Posada-Asinara Shear Zone (NE Sardinia, Italy). Geosciences 10, 288, doi:10.3390/geosciences10080288.

Carosi, R., Frassi, C., Montomoli, C., 2009. Deformation during exhumation of medium and high-grade metamorphic rocks in the Variscan chain in Northern Sardinia (Italy). Geol. J. 44 (3), 280–305.

Carosi, R., Montomoli, C., Tiepolo, M., Frassi, C., 2012. Geochronological constraints on post-collisional shear zones in the Variscides of Sardinia (Italy). Terra Nova 24, 42–51.

Casini, L., Puccini, A., Cuccuru, S., Maino, M., Oggiano, G., 2013. GEOTHERM: a finite difference code for testing metamorphic P–T–t paths and tectonic models. Comp. Geosci. 59, 171–180.

Cocherie, A., Albarede, F., 2001. An improved U-Th-Pb age calculation for electron microprobe dating of monazite. Geochim. Cosmochim. Acta 65(24), 4509–4522.

Connolly, J.A.D., Memmi, I., Trommsdorff, V., Franceschelli, M., Ricci, C.A., 1994. Forward modeling of calc-silicate microinclusions and fluid evolution in a graphitic metapelite, northeast Sardinia. Am. Mineral. 79, 960–972.

Connolly, J.A.D., 2009. The geodynamic equation of state: what and how. Geochem. Geophys. Geosyst. 10, Q10014.

Cortesogno, L., Gaggero, L., Oggiano, G., Paquette, J.-L., 2004. Different tectono-thermal evolutionary paths in eclogitic rocks from the axial zone of the Variscan chain in Sardinia (Italy) compared with the Ligurian Alps. Ofioliti 29, 125–144.

Cruciani, G., Franceschelli,M., Groppo, C., Oggiano, G., Spano, M.E., 2015b. Re-equilibration history and P-T path of eclogites from Variscan Sardinia, Italy: a case study from the medium-grade metamorphic complex. Int. J. Earth Sci. 104, 797–814.

Cruciani, G., Franceschelli, M., Langone, A., Puxeddu, M., Scodina, M., 2015c. Nature and age of pre-Variscan eclogite protoliths from the Low- to Medium-Grade Metamorphic Complex of north–central Sardinia (Italy) and comparisons with coeval Sardinian eclogites in the northern Gondwana context. J. Geol. Soc. Lond. 172, 792–807.

Cruciani, G., Montomoli, C., Carosi, R., Franceschelli, M., Puxeddu, M., 2015a. Continental collision from two perspectives: a review of Variscan metamorphism and deformation in northern Sardinia. Per. Mineral. 84, 657–699.

Cruciani, G., Franceschelli, M., Massonne, H.-J., Carosi, R., Montomoli, C., 2013. Pressure-temperature and deformational evolution of high-pressure metapelites from Variscan NE Sardinia, Italy. Lithos 175-176, 272–284.

Cruciani, G., Dini, A., Franceschelli, M., Puxeddu, M., Utzeri, D., 2010. Metabasite from the Variscan belt in NE Sardinia, Italy: within-plate OIB-like melts with very high Sr and low Nd isotope ratios. Eur. J. Mineral. 22, 509–523.

Cruciani, G., Franceschelli, M., Groppo, C., 2011. P-T evolution of eclogite-facies metabasite from NE Sardinia, Italy: insights into the prograde evolution of Variscan eclogites. Lithos 121, 135–150.

Cruciani, G., Franceschelli, M., Massonne, H.-J., Musumeci, G., Spano, M.E., 2016. Thermomechanical evolution of the high-grade core in the nappe zone of Variscan Sardinia, Italy: the role of shear deformation and granite emplacement. J. metamorphic Geol. 34, 321–342.

Cruciani, G., Fancello, D., Franceschelli, M., Scodina, M., Spano, M.E., 2014a. Geothermobarometry of Al-silicate-bearing migmatites from the Variscan chain of NE Sardinia, Italy: a P-T pseudosection approach. Per. Mineral. 83 (1), 19–40.

Cruciani, G., Franceschelli, M., Caironi, V., Musumeci, G., 2020. U–Pb ages on detrital zircons and geochemistry of Lula paragneiss from Variscan belt, NE Sardinia, Italy: implications for source rocks and early Paleozoic paleogeography. Ital. J. Geosci. 139, 131–148.

Cruciani, G., Franceschelli, M., Foley, S.F., Jacob, D.E., 2014b. Anatectic amphibole and restitic garnet in some Variscan migmatite from NE Sardinia, Italy: insights into partial melting from mineral trace elements. Eur. J. Mineral. 26, 381–395.

Cruciani, G., Franceschelli, M., Puxeddu, M., Tiepolo, M., 2018. Metavolcanics from Capo Malfatano, SW Sardinia, Italy: New insight on the age and nature of Ordovician volcanism in the Variscan foreland zone. Geol. J. 53, 1573–1585.

Cruciani, G., Fancello, D., Franceschelli, M., Musumeci, G., 2019. Geochemistry of the Monte Filau orthogneiss (SW Sardinia, Italy): insight into the geodynamic setting of Ordovician felsic magmatism in the N/NE Gondwana margin.. Italian J. Geosci. 138, 136–152.

Cruciani, G., Franceschelli, M., Massonne, H.-J., Musumeci, G., 2021. Evidence of two metamorphic cycles preserved in garnet from felsic granulite in the southern Variscan belt of Corsica, France. Lithos 380–381, 105919.

Di Vincenzo, G., Carosi, R., Palmeri, R., 2004. The relationship between tectono-metamorphic evolution and argon isotope records in white mica: constraints from in situ 40Ar–39Ar laser analysis of the Variscan basement of Sardinia. J. Petrol. 45, 1013–1043.

Edel, J. B., Schulmann, K., Lexa, O., Lardeaux, J. M., 2018. Late Palaeozoic palaeomagnetic and tectonic constraints for amalgamation of Pangea supercontinent in the European Variscan belt. Earth-Sci. Rev. 177, 589–612.

Elter, F.M., Padovano, M., Kraus, R.K., 2010. The Variscan HT metamorphic rocks emplacement linked to the interaction between Gondwana and Laurussia plates: structural constraints in NE Sardinia (Italy). Terra Nova 22, 369–377.

Engi, M., Lanari, P., Kohn, M.J., 2017. Significant Ages—An Introduction to Petrochronology. Rev. Mineral. Geochem. 83 (1), 1–12.

Fancello, D., Cruciani, G., Franceschelli, M., Massonne, H.-J., 2018. Trondhjemitic leucosomes in paragneisses from NE Sardinia: geochemistry and P-T conditions of melting and crystallization. Lithos 304-307, 501–517.

Faryad, S.W., Baldwin, S.L., Jedlicka, R., Ježek, J., 2019. Two‐stage garnet growth in coesite eclogite from the southeastern Papua New Guinea (U)HP terrane and its geodynamic significance. Contrib. Mineral. Petrol. 174, 73, DOI: doi.org/10.1007/s00410-019-1612-4.

Faryad, S.W., Cuthbert S.J., 2020. High-temperature overprint in (U)HPM rocks exhumed from subduction zones; A product of isothermal decompression or a consequence of slab break-off (slab rollback)? Earth-Sci. Rev. 202, 103108.

Faryad, S.W., Ježek, J., 2019. Compositional zoning in garnet and its modification by diffusion during pressure and temperature changes in metamorphic rocks; an approach and software. Lithos 332–333, 287–295.

Ferry, J.M., Watson, E.B., 2007. New thermodynamic models and revised calibrations for the Ti-in-zircon and Zr-in-rutile thermometers. Contrib. Mineral. Petrol. 154, 429–437.

Franceschelli, M., Memmi, I., Pannuti, F., Ricci, C. A., 1989. Diachronous metamorphic equilibria in the Hercynian basement of northern Sardinia, Italy. In Daly, J. S., Cliff, R. A., and Yardley, B.W. D., (eds.), Evolution of Metamorphic Belts, Geol. Soc. London, Special Publ. 43, 371–375.

Franceschelli, M., Puxeddu, M., Cruciani, G., Dini, A., Loi, M., 2005. Layered amphibolite sequence in NE Sardinia, Italy: remnant of a pre-Variscan mafic silicic layered intrusion? Contrib. Mineral. Petrol. 149, 164–180.

Frassi, C., Carosi, R., Montomoli, C., Law, R.D., 2009. Kinematics and vorticity of flow associated with post-collisional oblique transpression in the Variscan Axial Zone of northern Sardinia (Italy). J. Struct. Geol. 31, 1458–1471.

George, F.R., Waters, D.J., Gough, S.J., Searle, M.P., Forshaw, J.B., 2020. Phase equilibria and microstructural constraints on the high-T building of the Kohistan island arc: The Jijal garnet granulites, northern Pakistan. J. metamorphic Geol. 00, 1–30. DOI: 10.1111/jmg.12622

Gaidies, F., De Capitani, C., Abart, R., 2008. THERIA_G: a software program to numerically model prograde garnet growth. Contrib. Mineral. Petrol. 155, 657–671.

Ganade, C.E., Lanari, P., Rubatto, D., Hermann, J., Weinberg, R.F., Basei, M.A.S., Tesser, L.R., Caby, R., Agbossoumondè, Y., Ribeiro, C.M., 2021. Magmatic flare-up causes crustal thickening at the transition from subduction to continental collision. Communications Earth & Environment. DOI: 10.1038/s43247-021-00103-z.

Graziani, R., Montomoli, C., Iaccarino, S., Menegon, L., Nania, L., Carosi, R., 2020. Structural setting of a transpressive shear zone: Insights from geological mapping, quartz petrofabric and kinematic vorticity analysis in NE Sardinia (Italy). Geol. Mag. 157, 1898–1916.

Helbing, H., Frisch, W., Bons, P.D., 2006. South Variscan terrane accretion: Sardinian constraints on the intra-Alpine Variscides. J. Structural Geol. 28, 1277–1291.

Helbing, H., Tiepolo, M., 2005. Age determination of Ordovician magmatism in NE Sardinia and its bearing on Variscan basement evolution. J. Geol. Soc. London 162, 689–700.

Holland, T.J.B., Powell, R., 1998. An internally consistent thermodynamic data set for phases of petrological interest. J. metamorphic Geol. 16, 309–343.

Holland, T.J.B., Baker, J.M., Powell, R., 1998. Mixing properties and activity-composition relationships of chlorites in the system MgO-FeO-Al_2O_3-SiO_2-H_2O. Eur. J. Mineral. 10, 395–406.

Janoušek, V., Holub, F.V., 2007. The causal link between HP-HT metamorphism and ultrapotassic magmatism in collisional orogens: case study from the Moldanubian zone of the Bohemian Massif. Proc. Geol. Assoc. 118, 75–86.
Kulhánek, J., Faryad, S.W., Jedlicka, R., Svojtka, M., 2021. Dissolution and reprecipitation of garnet during eclogite-facies metamorphism; major and trace element transfer during atoll garnet formation. J. Petrol. 62(11), 1–22.
Kohn, M.J., 2020. A refined zirconium-in-rutile thermometer. Am. Mineral. 105, 963–971.
Li, B., Massonne, H.-J., Opitz, J., 2017. Clockwise and anticlockwise P-T paths of high-pressure rocks from the 'La Pioza' eclogite body of the Malpica-Tuy zone, NW Spain. J. Petrol. 58, 1363–1392.
Liu, P.L., Massonne, H.-J., 2019. An anticlockwise P-T path at high-pressure, high-temperature conditions for a migmatitic gneiss from the island of Fjørtoft, Western Gneiss Region, Norway, indicates two burial events during the Caledonian orogeny. J. metamorphic Geol. 37, 567–588.
Massonne, H.-J., 2012. Formation of amphibole and clinozoisite-epidote in eclogite owing to fluid infiltration during exhumation in a subduction channel. J. Petrol. 53, 1969–1998.
Massonne, H.-J., Li, B., 2020. Zoning of eclogitic garnet cores – a key pattern demonstrating the dominance of tectonic erosion as part of the burial process of worldwide occurring eclogites. Earth-Science Revi. 210, 103356, doi.org/10.1016/j.earscirev.2020.103356.
Massonne, H.-J., Cruciani, G., Franceschelli, M., Musumeci, G., 2018. Anticlockwise pressure–temperature paths record Variscan upper-plate exhumation: example from micaschists of the Porto Vecchio region, Corsica. J. metamorphic Geol. 36, 55–77.
Massonne, H.-J., Cruciani, G., Franceschelli, M., 2013. Geothermobarometry on anatectic melts – a high-pressure Variscan migmatite from Northeast Sardinia. Int. Geol. Rev. 55, 1490–1505.
Matte, P., 1986. Tectonics and plate tectonics model for the Variscan belt of Europe. Tectonophysics 126, 329–374.
Montomoli, C., Iaccarino, S., Carosi, R., Langone, A., Visonà, D., 2013. Tectonometamorphic discontinuities within the Greater Himalayan Sequence in Western Nepal (Central Himalaya): Insights on the exhumation of crystalline rocks. Tectonophysics 608, 1349–1370.
Palmeri, R., Fanning, M., Franceschelli, M., Memmi, I., Ricci, C.A., 2004. SHRIMP dating of zircons in eclogite from the Variscan basement in north-eastern Sardinia (Italy). Neues Jahrb. Mineral., Monat. 6, 275–288.

Ricci, C.A., Carosi, R., Di Vincenzo, G., Franceschelli, M., Palmeri, R., 2004. Unravelling the tectono-metamorphic evolution of medium-pressure rocks from collision to exhumation of the Variscan basement of NE Sardinia: a review. Special issue 2: a showcase of the Italian research in metamorphic petrology. Per. Mineral. 73, 73–83.

Rossi, P., Cocherie, A., 1991. Genesis of a Variscan batholith: field, mineralogical and geochemical evidence from the Corsica–Sardinia batholith, in: The European Geotraverse, Part 7, Tectonophysics 195, 319–346.

Rossi, P., Oggiano, G., Cocherie, A., 2009. A restored section of the “southern Variscan realm” across the Corsica–Sardinia microcontinent. CR Geoscience 341, 224–238.

Schneider, J., Corsini, M., Reverso-Peila, A., Lardeaux, J.M., 2014. Thermal and mechanical evolution of an orogenic wedge during Variscan collision: an example in the Maures-Tanneron Massif (SE France). In: The Variscan Orogeny: Extent, Timescale and the Formation of the European Crust. Schulmann K., Martínez Catalán J.R., Lardeaux J.M., Janoušek V. and Oggiano G. (eds.): Geological Society of London, Special Publ. 405, 313–331.

Scodina, M., Cruciani, G., Franceschelli, M., Massonne, H.-J., 2019. Anticlockwise P-T evolution of amphibolites from NE Sardinia, Italy: Geodynamic implications for the tectonic evolution of the Variscan Corsica-Sardinia block. Lithos 324, 763–775.

Scodina, M., Cruciani, G., Franceschelli, M., Massonne, H.-J., 2020. Multilayer corona textures in the high-pressure ultrabasic amphibolite of Mt. Nieddu, NE Sardinia (Italy): Equilibrium versus disequilibrium. Per. Miner. 89, 169–186.

Scodina, M., Cruciani, G., Franceschelli, M., 2021. Metamorphic evolution and P–T path of the Posada Valley amphibolites: new insights on the Variscan high pressure metamorphism in NE Sardinia, Italy. C.R. Geoscience 353(1), 227–246.

Simonetti, M., Carosi, R., Montomoli, C., Corsini, M., Petroccia, A., Cottle, J.M., Iaccarino, S., 2020. Timing and kinematics of flow in a transpressive dextral shear zone, Maures Massif (Southern France). Int. J. Earth Sci. 109, 2261–2285.

Simonetti, M., Carosi, R., Montomoli, C., Langone, A., D’addario, E., Mammoliti, E., 2018. Kinematic and geochronological constraints on shear deformation in the Ferriere-Mollières shear zone (Argentera-Mercantour Massif, Western Alps): Implications for the evolution of the Southern European Variscan Belt. Int. J. Earth Sci. 107, 2163–2189.

Simonetti, M., Carosi, R., Montomoli, C., Law R.D., Cottle J. M., 2021. Unravelling the development of regional-scale shear zones by a multidisciplinary approach: The case study of the Ferriere-Mollières Shear Zone (Argentera Massif, Western Alps). J. Struct. Geol. 149, 104399.

Thiessen, E.J., Gibson, H.D., Regis, D., Pehrsson, S.J., Ashley, K.T., Smit, M.A., 2019. The distinct metamorphic stages and structural styles of the 1.94–1.86 Ga Snowbird Orogen, Northwest Territories, Canada. J. metamorphic Geol. 38, 963–992.

Tomkins, H.S., Powell, R., Ellis, D.J., 2007. The pressure dependence of the zirconium-in rutile thermometer. J. metamorphic Geol. 25, 703–713.

Watson, E. B., Wark, D. A., Thomas, J. B., 2006. Crystallization thermometers for zircon and rutile. Contrib. Mineral. Petrol. 151,413–433.

White, R. W., Powell, R., Holland, T. J. B., Johnson, T. E., Green, E.C.R., 2014. New mineral activity–composition relations for thermodynamic calculations in metapelitic systems. J. Metamorph. Geol. 32, 261–286.

Whitney, D.L., Evans, B.W., 2010. Abbreviations for names of rock-forming minerals. Am. Mineral. 95, 185–187.

Williams, M.L., Jercinovic, M.J., 2012 Tectonic interpretation of metamorphic tectonites: integrating compositional mapping, microstructural analysis and in situ monazite dating. J. metamorphic Geol. 30,739–752.

Zack, T., Moraes, R., Kronz, A., 2004. Temperature dependence of Zr in rutile: empirical calibration of a rutile thermometer. Contrib. Mineral. Petrol. 148, 471–488.

Figure Captions

Fig. 1. a) Tectonic sketch map of the Variscan chain of Sardinia (the arrow refers to the area shown in b); b) Simplified geological map of NE Sardinia metamorphic basement modified from Cruciani et al. (2020) and references therein. Sample location (red asterisk) is also shown. 1: recent (a) and Mesozoic (b) sediments; 2: Variscan granitoids, with felsic (c) and mafic (d) dikes; 3: Migmatite of the Sil+Ms/Sil+Kfs zones with retrogressed eclogite (e) and orthogneiss (f); 4: Micaschist and gneiss of the St+Bt/Ky+Bt zones, mylonite and amphibolite (g); 5: Granodioritic orthogneiss and augen gneiss; 6: Micaschist and paragneiss of the Grt+Ab/oligoclase zone; 7: Phyllite and metasandstone of the Bt zone; 8: Foliation; 9: Fold axes; 10: Fault.

Fig. 2. a) Silver-coloured mylonitic micaschist with garnet and staurolite porphyroblasts homogeneously distributed in the rock matrix; b) Thin section photo-scan of micaschist sample FZ13. Mineral abbreviations after Whitney and Evans (2010).

Fig. 3. Photomicrographs and BSE images showing the relevant microstructures of the studied micaschist from NE Sardinia. a) Snowball garnet with quartz microinclusions forming a sigmoidal

pattern; Sample FD3X; b) Staurolite wrapped by the S2 schistosity; Sample FD3X; c) Staurolite bordered by strain shadows filled by chlorite and muscovite. Sample FZ13; d) Plagioclase preserving a poorly-defined pre-D2 relic foliation (dotted white line) wrapped by the S2 schistosity. Sample FZ13; e) Microinclusions in a garnet porphyroblast showing a sigmoidal- to spiral-shaped arrangement of an earlier S1 schistosity preserved inside the garnet. Sample FD3X; f) Garnet with core and rim domains, distinguishable by the size and distribution of its microinclusions; quartz inclusions in the rim domain are bigger than those preserved in the core. Sample FZ13; g) Detail of chloritoid armoured in the rim of the garnet shown in Fig. 4b; h) Staurolite with quartz and ilmenite inclusions. Strain shadows at both sides of the crystal are filled by chlorite. Sample FZ13.

Fig. 4. Metamorphic evolution scheme inferred from microstructural relationships and mineral assemblages with special reference to garnet and staurolite porphyroblasts, mineral inclusions, and surrounding S2-oriented matrix. Wmca: white mica (including muscovite and paragonite).

Fig. 5. X-ray Mg, Ca, Mn and Fe concentration maps of garnet porphyroblasts. Warm colours refer to high concentrations, whereas cold colours refer to low concentrations. The garnet at the top (which is also recognizable in Fig. 3a) is from sample FZ13 whereas the garnet at the bottom is from sample FD3X. A-B trace in the Mn-map of garnet from FD3X shows the measuring points for the compositional profile shown in Fig. 7c.

Fig. 6. Chemical composition in terms of molar fraction of grossular (+ andradite) versus that of pyrope (X_{Mg}) and spessartine (X_{Mn}) for: a) the garnet shown in Fig. 5a (sample FZ13) and b) the garnet shown in Fig. 5b (sample FD3X); c) Rim-core-rim compositional profile across the A-B trace of garnet porphyroblast in Fig. 5b.

Fig. 7. EMP spot analyses of white mica from samples FZ13 and FD3X in terms of Si contents vs. those of Na, Fe, Mg and Ti cations.

Fig. 8. (a) P–T pseudosection in the NCKFMASH + Mn + Ti system calculated for the bulk composition of micaschist sample FZ13. A few small P–T fields are not assigned to a mineral assemblage; (b) Compositional isopleths for grossular (X_{Ca}) component in garnet; (c) Compositional isopleths for almandine (X_{Fe}) component; (d) Compositional isopleths for spessartine (X_{Mn}) component; (e) Isomodes showing garnet content (vol.%); (f) Compositional isopleths showing Si content (apfu, based on 11 oxygens) and X_{Mg} ratio (red dotted line) in K-white mica.

Fig. 9. (a) and (b) Some selected compositional isopleths for garnet components, Si (apfu) content in muscovite, and X_{Mg} in chloritoid and staurolite for the P-T pseudosections shown in Fig. 8a for sample FZ13 and in Fig. S2a for sample FD3X. Intersecting red and blue lines refer to garnet core and rim compositions. Solid, dashed, and dotted lines refer to grossular, almandine and spessartine

components. (a) and (b) traces in the P-T path are the stages along the initial garnet profiles shown in Fig. 10 are calculated.

Fig. 10. Best fits between the measured (dots) and initial modelled profiles (colored lines) in garnet, calculated by CZGM software along the P-T traces (a) and (b) shown in Fig. 9 for samples FZ13 and FD3X.

Fig. 11. Sketch of the proposed tectonic evolution of the Sardinian Variscides. a) Convergence between Gondwana and Armorica: subduction of the oceanic lithosphere where oceanic crust records HP-LT conditions; b) collision stage at c. 360–340 Ma; tectonic dismembering and transport to the South of the suture. Start of the D1 tectonic phase in the continental crust and exhumation of HP–LT oceanic crust slices by (late) D1 sinistral shearing. At the same time the more distal portions of the continental crust are underthrusted reaching HP–LT conditions comparable with the ones recorded in the oceanic crust. Red asterisk: possible position of the study HP sample (this paper) in the continental crust; Yellow asterisk: possible position of the HP sample in the amphibolite derived from oceanic crust by Scodina et al. (2021).

Table captions

Table 1 Representative electron microprobe analyses of garnet, feldspar, staurolite, micas, chlorite and chloritoid in samples FZ13 and FD3X.

Table 2 Bulk–rock analyses (wt%) of samples FZ13 and FD3X determined by X-ray fluorescence (XRF) spectrometry and modified compositions for the calculation of P–T pseudosections (see text for explanation).

Table 3 Representative compositions (wt%) and ages of monazite in micaschist sample FZ13. The structural formula was calculated based on four oxygen atoms.

Supplementary material

Fig. S1. X-ray yttrium concentration maps for the garnet porphyroblasts shown in Fig. 5. Colour coding as in Fig. 5. Yellow arrows shows the Yttrium concentration jump.

Fig. S2. (a) P–T pseudosection in the NCKFMASH + Mn + Ti system calculated for the bulk composition of micaschist sample FD3X. A few small P–T fields are not assigned to a mineral assemblage; (b) Compositional isopleths for grossular (X_{Ca}) component in garnet; (c) Compositional isopleths for almandine (X_{Fe}) component; (d) Compositional isopleths for spessartine (X_{Mn}) component; (e) Isomodes showing garnet content (vol.%); (f) Compositional isopleths showing Si content (apfu, based on 11 oxygens) and X_{Mg} ratio (red dotted line) in K-white mica.

Fig. S3. Boundaries of the P-T stability fields for the most relevant mineral phases (garnet, chloritoid, lawsonite, staurolite, biotite, rutile, ilmenite) and compositional isopleths for X_{Mg} ratio in chloritoid of samples FZ13 and FD3X.

Fig. S4. Histograms showing results of the application of the Tomkins et al. (2007) and Kohn (2020) calibrations of the Zr-in-rutile geothermometer.

Fig. S5. Monazite ages (with error bars) plotted versus the different textural position of the analyzed grains. Synoptic table of tectonic and metamorphic events modified from Cruciani et al. (2015a) is also shown.

Table S1 EMP chemical analyses of rutile included in garnet, micaschist sample FZ13. TiO_2 was determined as difference from 100%. Temperatures based on Tomkins et al. (2007) and Kohn (2020).

Figure 1

Click here to access/download;Figure;Figure 1.tif

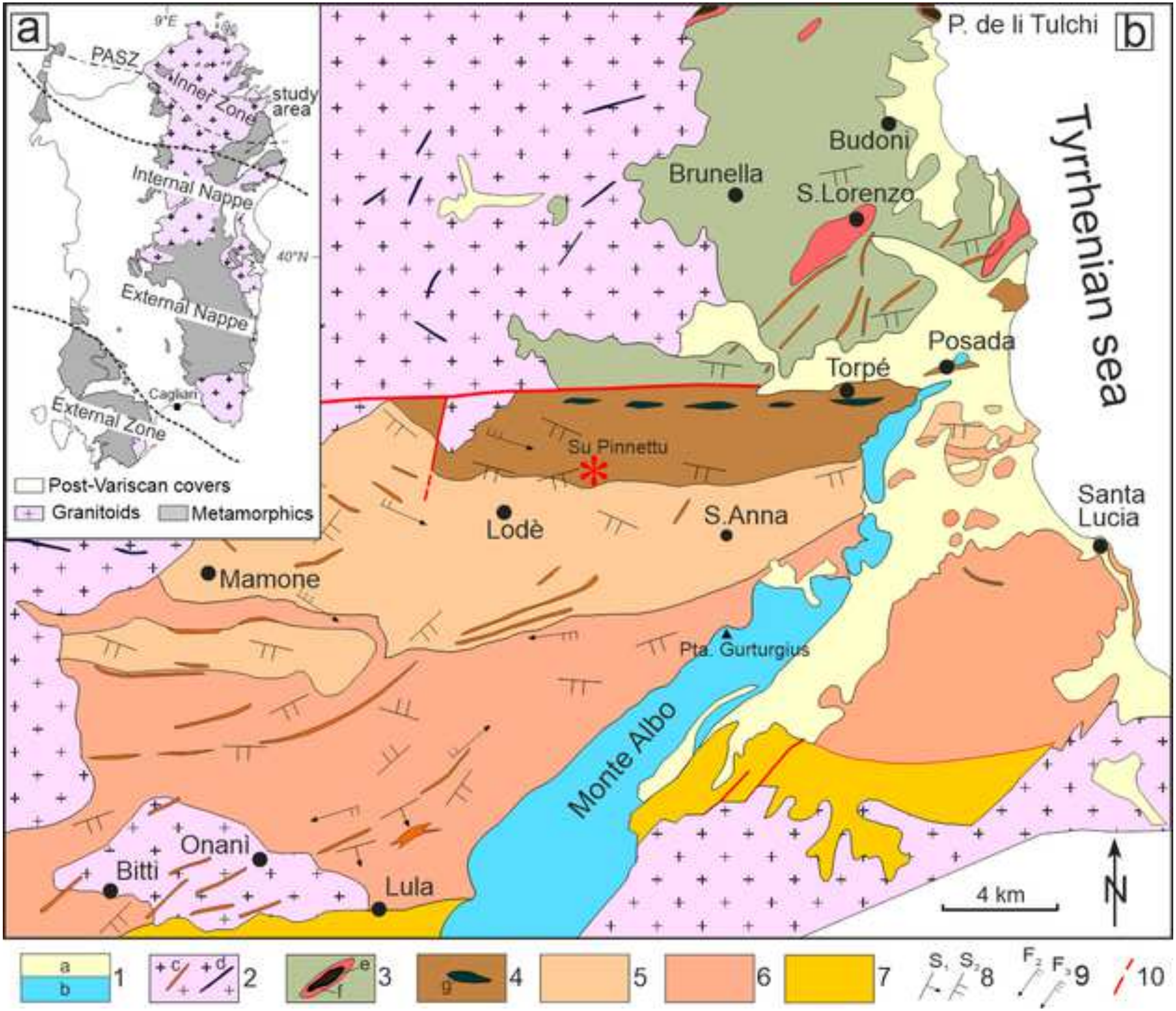

Figure 2

Click here to access/download;Figure;Figure 2.tif

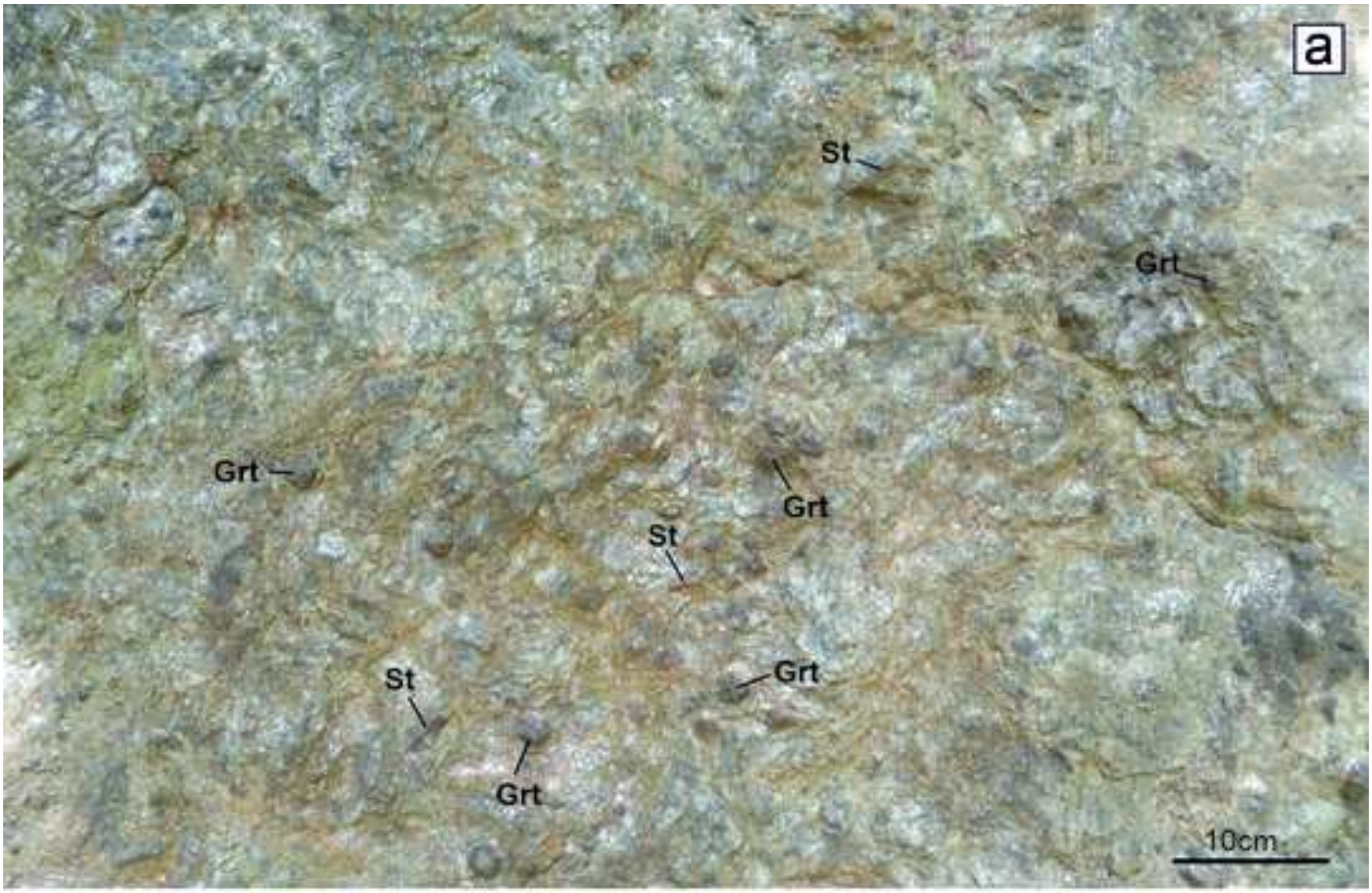

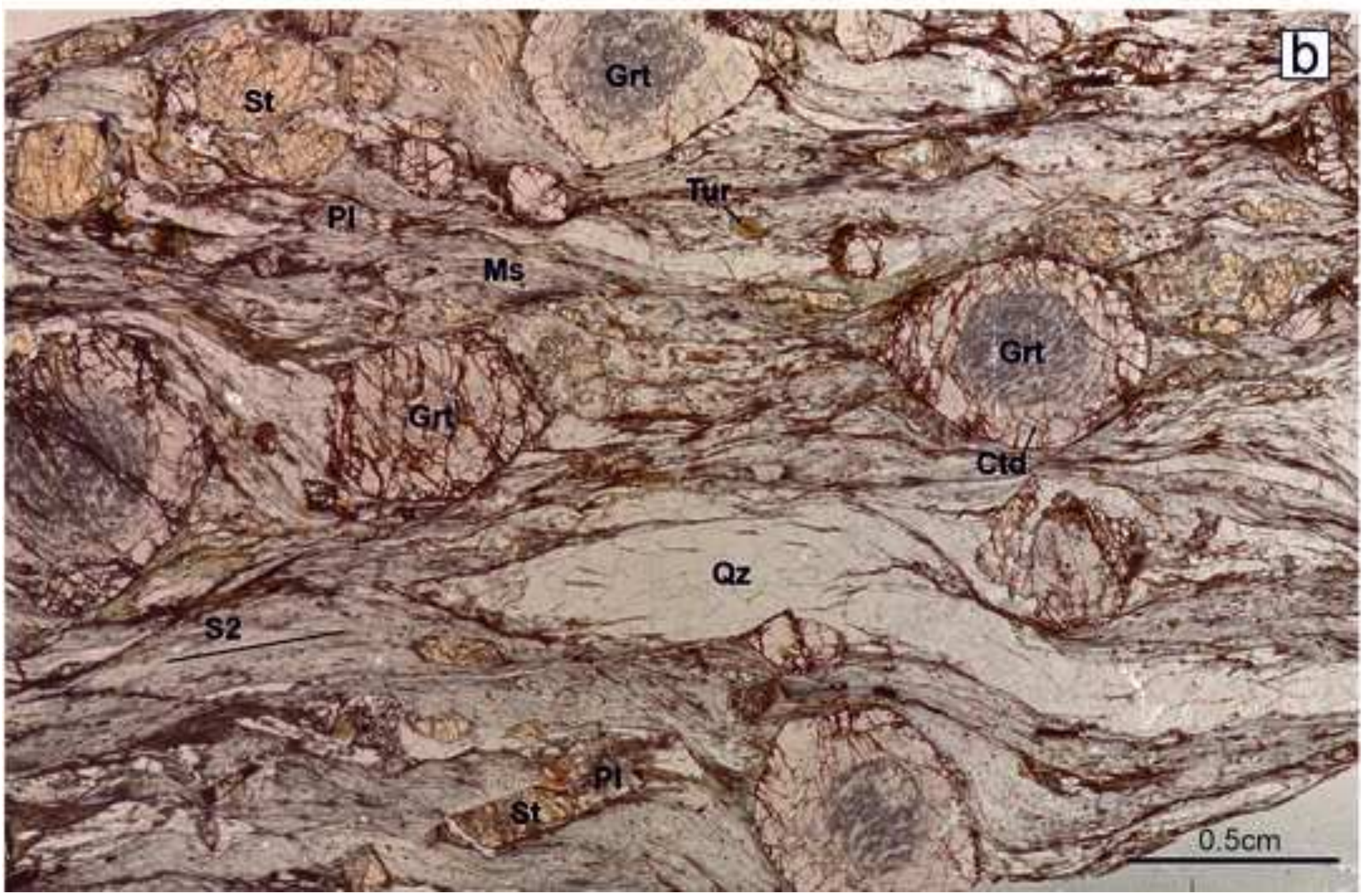

Figure 3

Click here to access/download;Figure;Figure 3.tif

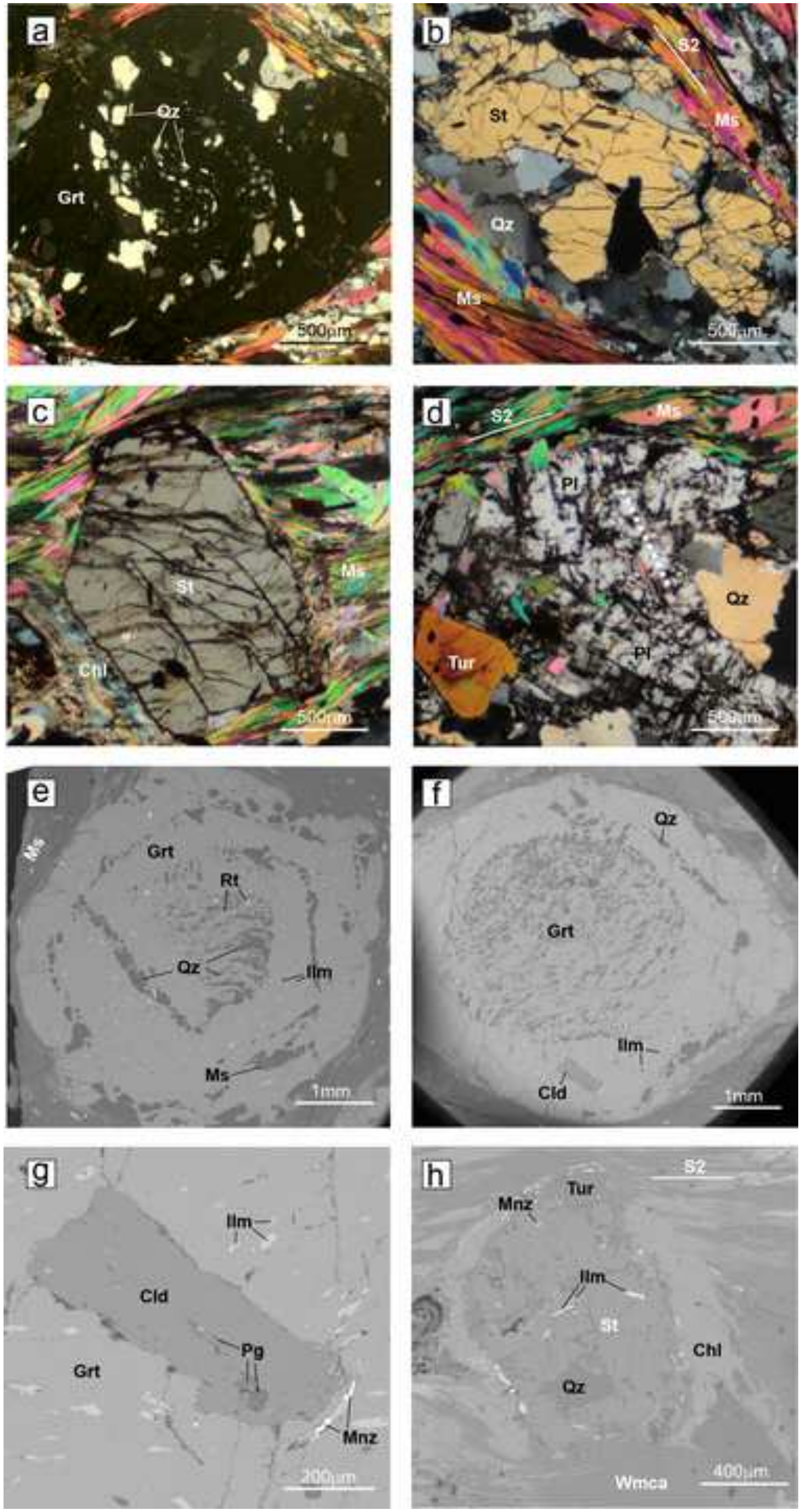

Figure 4

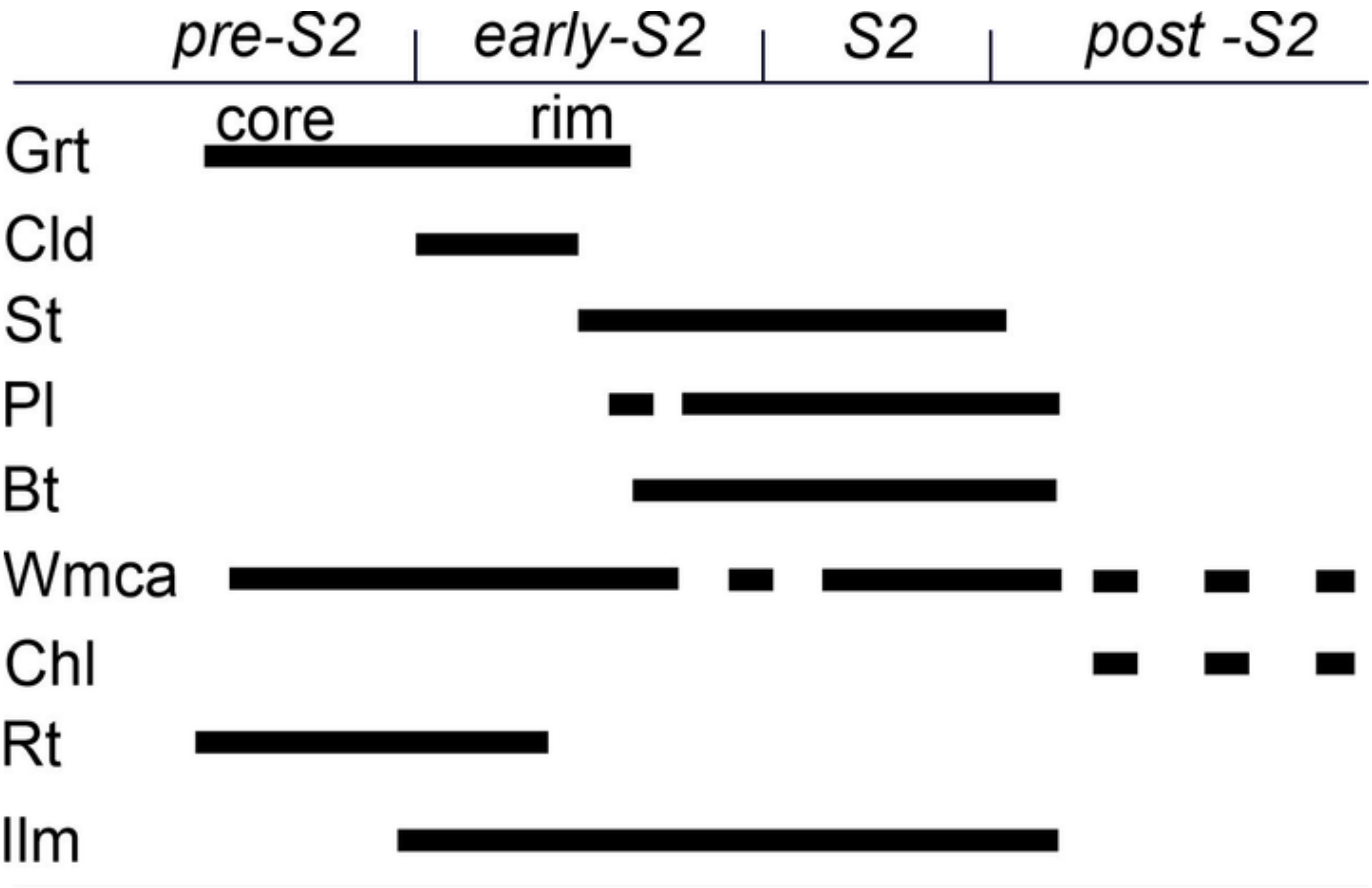
pre-S2
early-S2
S2
post -S2
core
rim
Grt
Cld
St
Pl
Bt
Wmca
Chl
Rt
Ilm

Figure 5 Click here to access/download;Figure;Figure 5.jpg

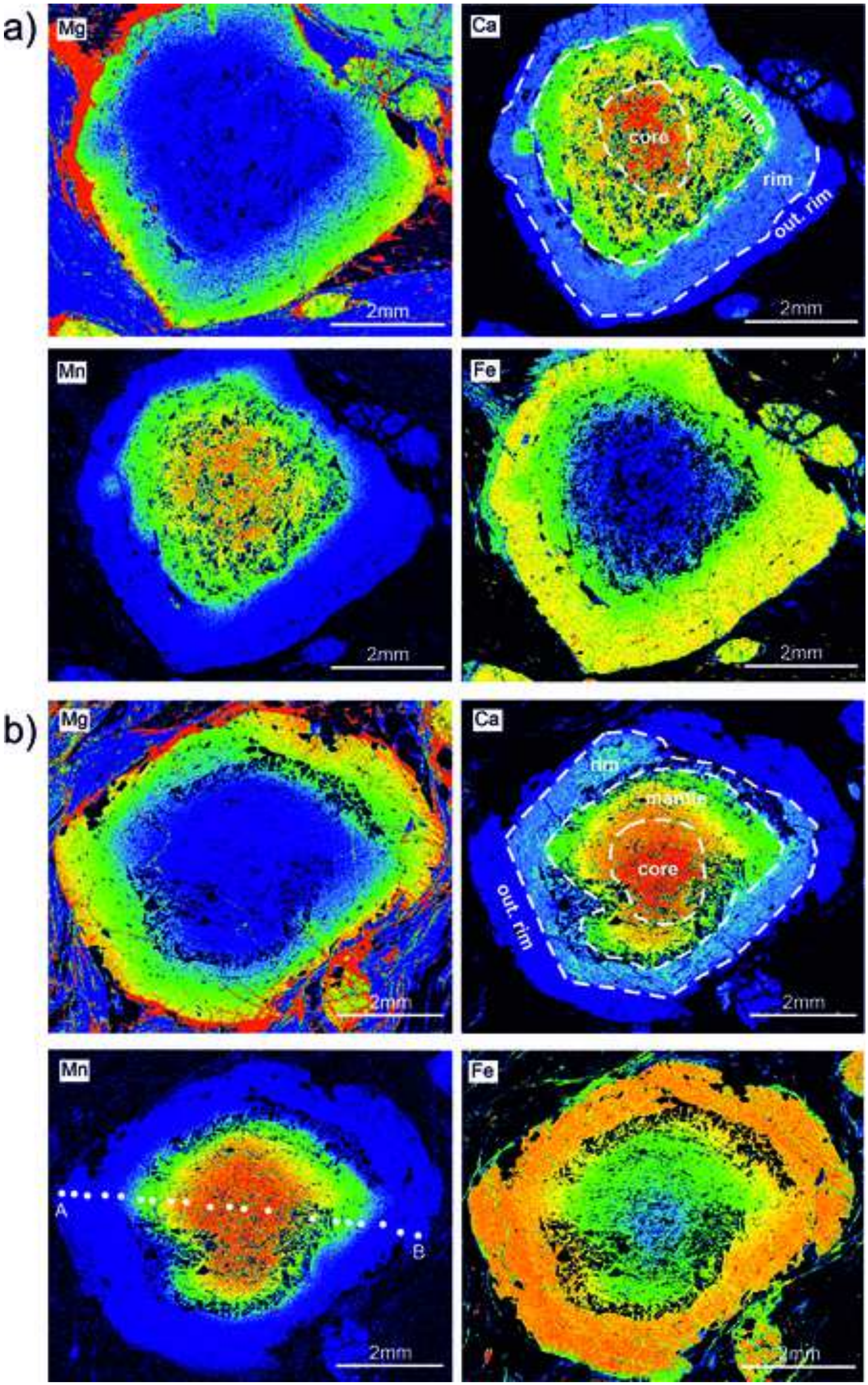

Figure 6

Click here to access/download;Figure;Figure 6.jpg

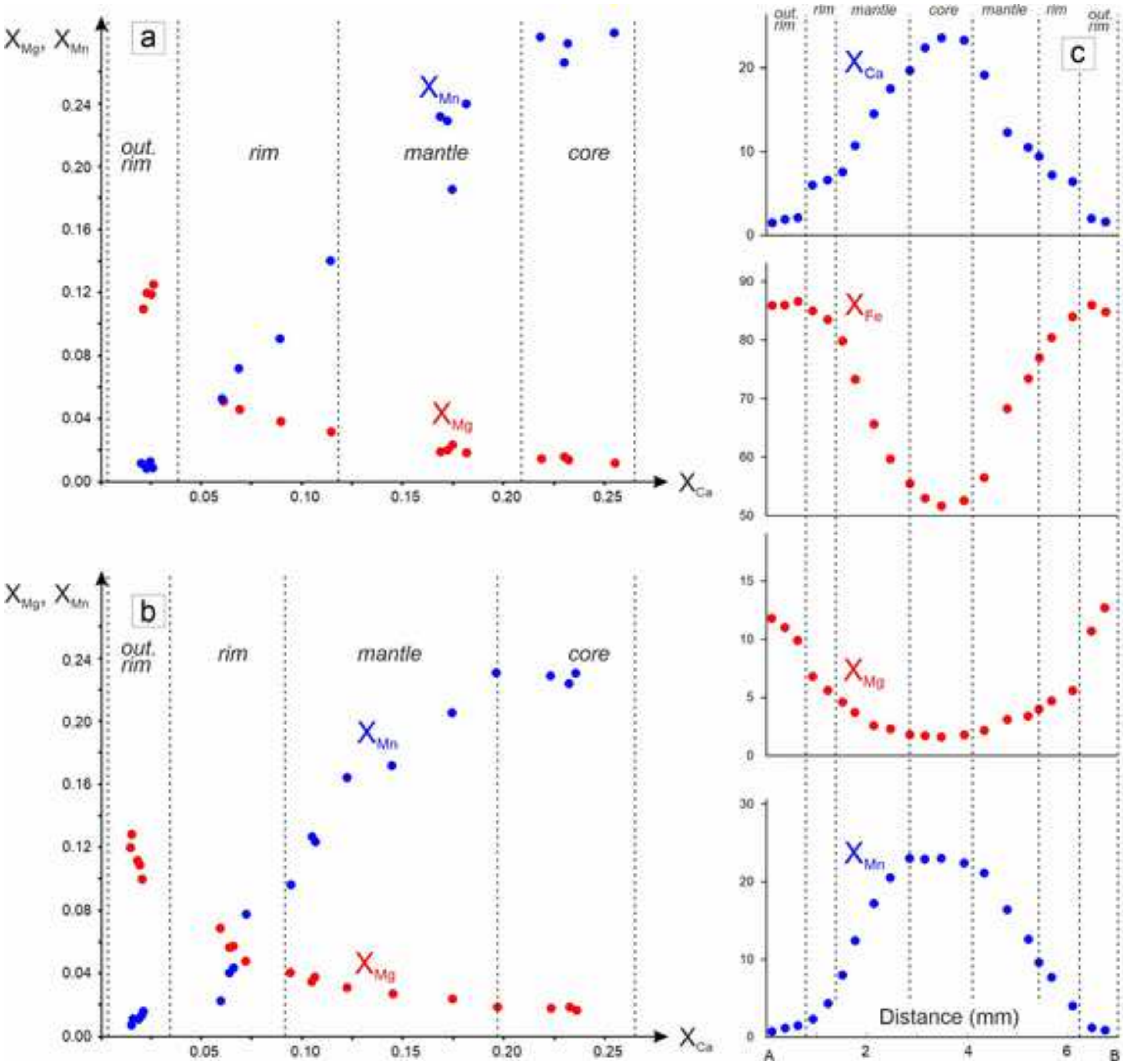

Figure 7

Click here to access/download;Figure;Figure 7.tif

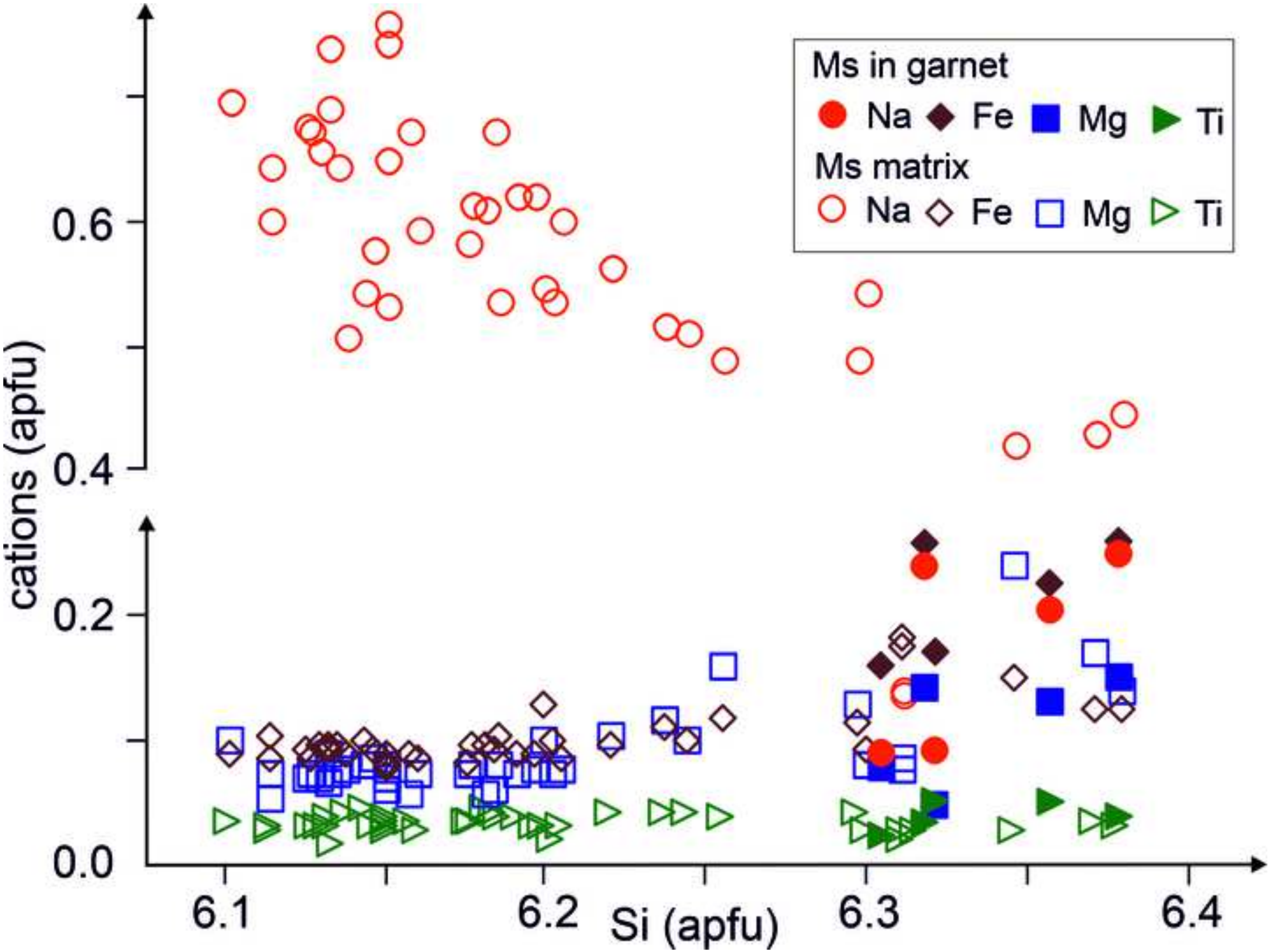

Figure 8

Click here to access/download;Figure;Figure 8.tif

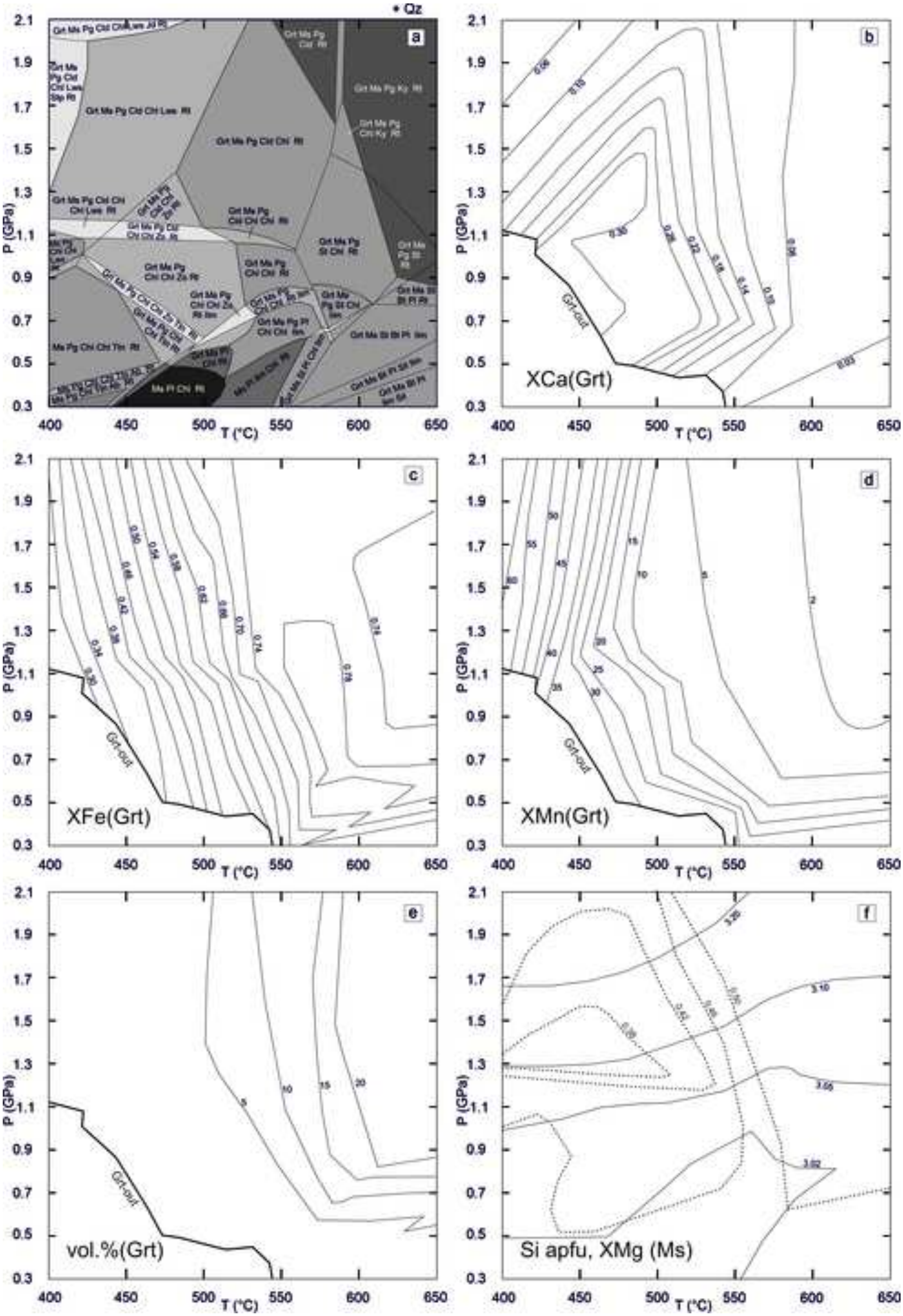

Figure 9

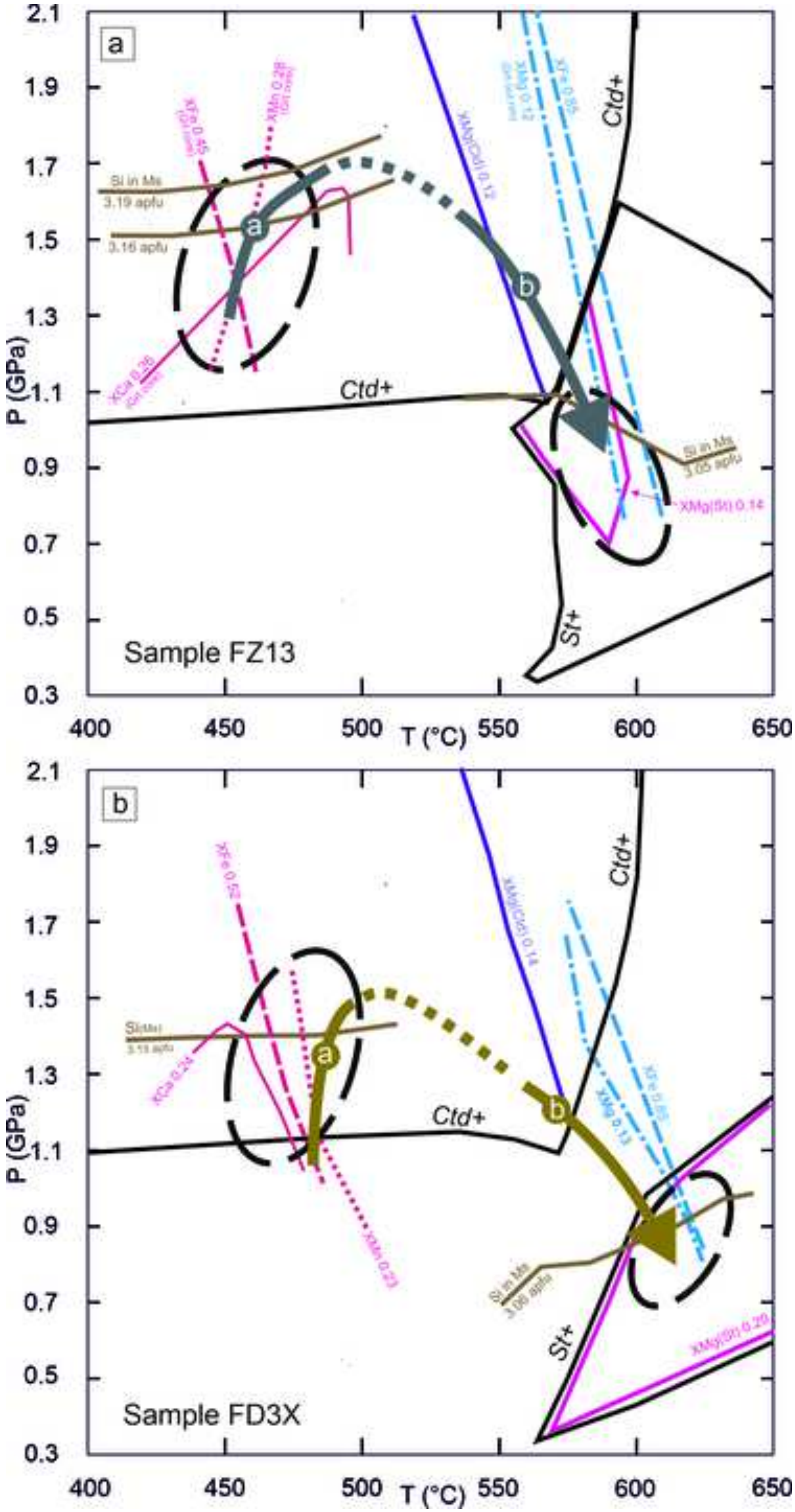
a
Sample FZ13
Ctd+
Ctd+
St+
Si in Ms
3.19 apfu
3.16 apfu
Si in Ms
3.05 apfu
XMg(St) 0.14
XMg(Ctd) 0.12
XFe 0.85
P (GPa)
T (°C)
b
Sample FD3X
Ctd+
Ctd+
St+
XFe 0.52
XMn 0.23
XCa 0.24
XMg(Ctd) 0.14
XMg 0.13
XFe 0.85
Si in Ms
3.06 apfu
XMg(St) 0.29
P (GPa)
T (°C)

Figure 10

Click here to access/download;Figure;Figure 10_ new.tif

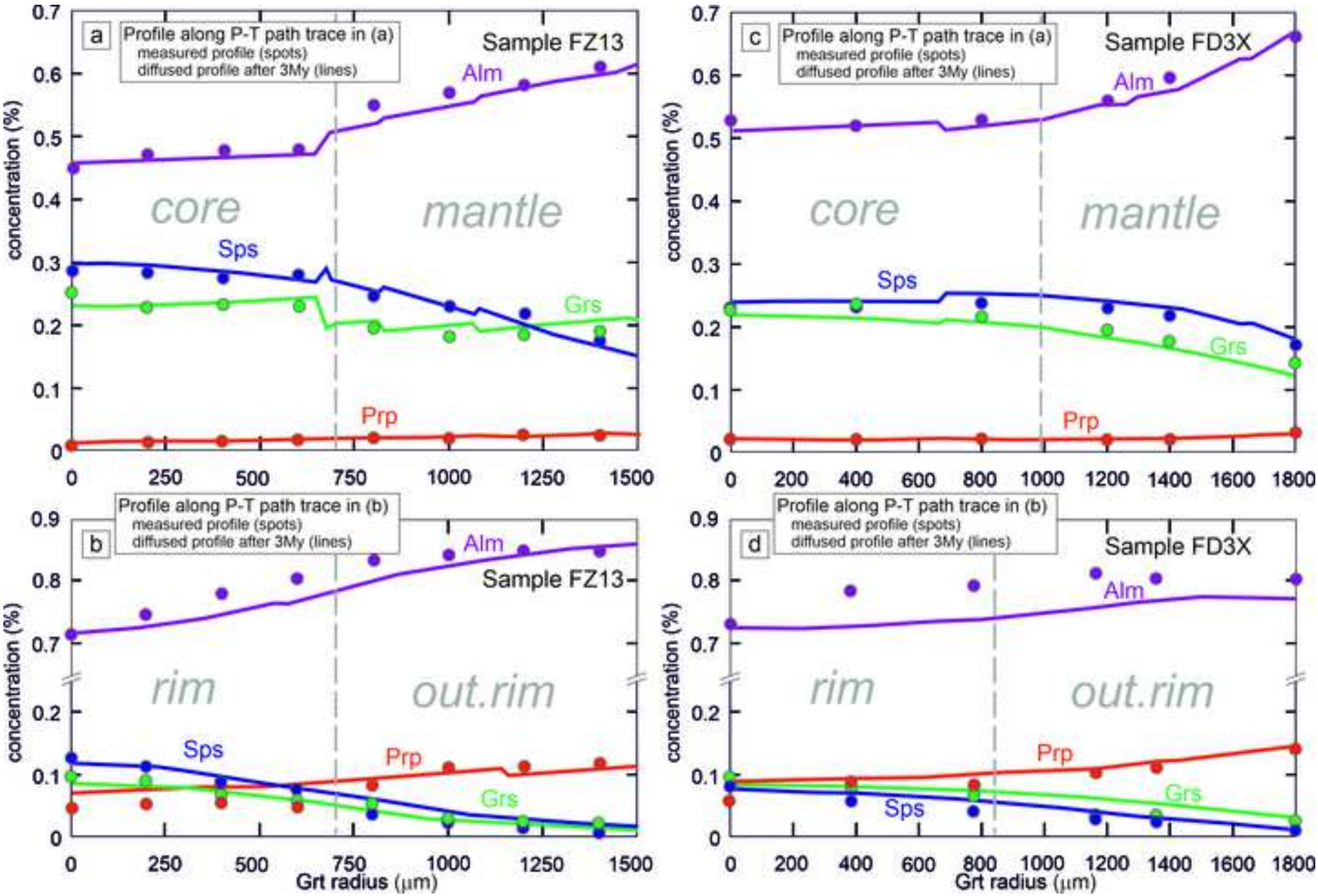

Figure 11

Click here to access/download;Figure;Figure 11.tif

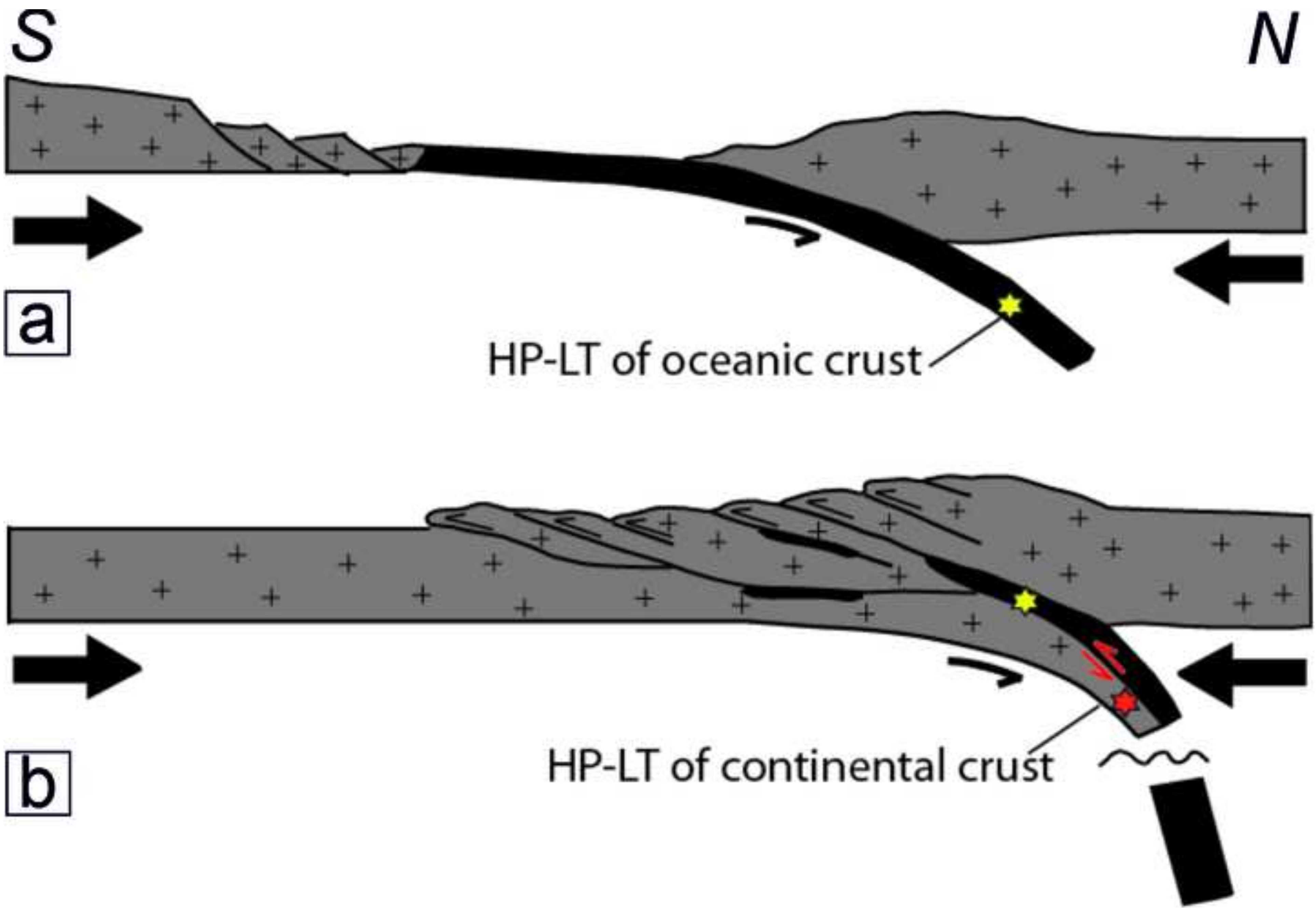

Table 1

Sample FZ13

	Grt core	mantle	rim	out. rim	Pl	St core	St rim	Ms in Gt	Ms in Gt	Ms mtx	Pg	Bt	Chl	Cld
SiO_2	36.71	36.63	36.11	36.89	65.74	28.05	27.07	47.79	47.04	46.02	44.76	35.13	23.63	24.11
TiO_2	0.21	0.19	0.06	0.05	-	0.57	0.55	0.33	0.30	0.32	0.09	1.48	0.06	-
Al_2O_3	20.77	20.81	20.76	21.18	20.93	54.78	56.17	33.00	33.37	36.44	40.90	18.86	22.51	40.51
FeO	20.76	26.32	37.73	38.33	0.04	13.56	13.20	2.30	2.32	0.79	1.03	20.28	30.71	26.12
Cr_2O_3	0.03	0.01	0.04	0.03	-	0.05	0.11	0.05	0.03	0.06	0.03	0.02	-	0.03
MnO	12.90	10.19	2.34	0.46	-	0.17	0.23	-	0.04	-	0.01	0.04	0.11	0.23
MgO	0.28	0.48	1.28	3.00	-	1.16	0.91	0.78	0.71	0.36	0.09	8.95	11.12	2.01
CaO	9.18	6.11	2.15	0.88	2.15	-	-	-	-	-	1.72	-	0.03	0.01
Na_2O	-	-	-	-	10.9	0.04	0.01	0.96	0.92	2.49	4.04	0.09	0.13	0.05
K_2O	-	-	-	-	-	-	0.01	9.83	9.96	7.74	1.35	9.59	0.02	-
Tot	100.84	100.74	100.47	100.82	99.76	98.38	98.26	95.04	94.69	94.22	94.02	94.44	88.32	93.07
Oxy	12	12	12	12	8	47	47	22	22	22	22	22	28	12
Si	2.96	2.96	2.95	2.97	2.90	7.89	7.62	6.38	6.32	6.11	5.81	5.43	5.10	1.99
Al	1.97	1.98	2.00	2.01	1.09	18.16	18.63	5.19	5.28	5.71	6.25	3.44	5.73	3.95
Ti	0.01	0.01	0.00	0.00	-	0.12	0.12	0.03	0.03	0.03	0.01	0.17	0.01	-
Fe^{2+}	1.39	1.78	2.58	2.57	0.00	3.19	3.11	0.26	0.26	0.09	0.11	2.62	5.55	1.81
Mn	0.88	0.70	0.16	0.03	-	0.04	0.06	-	0.01	-	0.00	0.01	0.02	0.02
Mg	0.03	0.06	0.16	0.36	-	0.49	0.38	0.15	0.14	0.07	0.02	2.06	3.58	0.25
Ca	0.79	0.53	0.19	0.07	0.10	-	-	-	-	-	0.24	-	0.01	0.00
Na	-	-	-	-	0.93	0.02	0.01	0.25	0.24	0.64	1.02	0.02	0.05	0.01
K	-	-	-	-	-	-	0.00	1.67	1.71	1.31	0.22	1.89	0.01	-
Alm	45	58	84	85	-	-	-	-	-	-	-	-	-	-
Prp	1	2	5	12	-	-	-	-	-	-	-	-	-	-
Grs	26	17	6	2	-	-	-	-	-	-	-	-	-	-
Sps	28	23	5	1	-	-	-	-	-	-	-	-	-	-
X_{Mg}	-	-	-	-	-	0.13	0.11	0.38	0.35	0.44	0.15	0.44	0.39	0.12
Ab	-	-	-	-	0.90	-	-	-	-	-	-	-	-	-

Table 1 Table 1 continued

Sample FD3X

	Grt core	mantle	rim	out. rim	Pl	St	Bt	Ms in Gt	Ms mtx	Cld
SiO_2	36.29	36.09	35.94	36.28	65.34	27.29	34.87	47.81	47.12	24.59
TiO_2	0.15	0.08	0.03	0.05	-	0.31	1.48	0.28	0.34	-
Al_2O_3	20.77	20.48	20.52	20.63	20.96	56.95	19.25	34.68	36.94	41.98
FeO	23.19	29.23	37.07	38.42	-	14.16	19.57	1.59	0.91	25.50
Cr_2O_3	0.04	0.00	0.02	-	-	0.07	-	0.01	0.09	-
MnO	10.19	7.54	1.89	0.32	-	0.43	0.05	0.14	-	0.32
MgO	0.41	0.66	1.4	2.96	-	1.28	9.36	0.38	0.34	2.38
CaO	8.26	5.04	2.28	0.53	2.19	0.02	0.01	-	0.01	-
Na_2O	0.04	-	-	0.05	10.85	-	0.17	0.53	2.58	-
K_2O	-	-	-	-	0.09	0.01	9.66	10.51	8.03	-
Tot	99.34	99.12	99.15	99.24	99.43	100.52	94.42	95.93	96.36	94.77
Oxy	12	12	12	12	8	47	22	22	22	12.00
Si	2.96	2.97	2.97	2.97	2.89	7.55	5.37	6.31	6.13	1.99
Al	1.99	1.99	1.99	1.99	1.09	18.56	3.49	5.39	5.67	4.01
Ti	0.01	0.00	0.00	0.00	-	0.06	0.17	0.03	0.03	-
Fe^{2+}	1.58	2.01	2.56	2.63	-	3.27	2.52	0.18	0.10	1.73
Mn	0.71	0.53	0.13	0.02	-	0.10	0.01	0.02	-	-
Mg	0.05	0.08	0.17	0.36	-	0.53	2.15	0.08	0.07	0.29
Ca	0.72	0.44	0.20	0.05	0.10	0.01	0.00	-	0.00	-
Na	0.01	-	-	0.01	0.93	-	0.05	0.14	0.65	-
K	-	-	-	-	0.01	0.00	1.90	1.77	1.33	-
Alm	52	66	84	86	-	-	-	-	-	-
Prp	2	3	6	12	-	-	-	-	-	-
Grs	24	14	7	2	-	-	-	-	-	-
Sps	23	17	4	1	-	-	-	-	-	-
X_{Mg}	-	-	-	-	-	0.14	0.46	0.31	0.41	0.14
Ab	-	-	-	-	0.90	-	-	-	-	-

Table 2

	FZ13			FD3X		
	Bulk	Bulk	Bulk minus	Bulk	Bulk	Bulk minus
	XRF	PERPLE_X	core&mant.	XRF	PERPLE_X	core&mant.
SiO_2	52.06	54.44	57.07	62.25	64.92	69.25
TiO_2	1.09	1.14	1.32	0.90	0.94	1.08
Al_2O_3	25.43	26.59	27.36	19.35	20.17	19.67
Fe_2O_3	10.88	-	-	8.09	-	-
FeO	-	10.24	6.49	-	7.60	3.05
MnO	0.24	0.25	-	0.16	0.17	-
MgO	1.70	1.78	1.91	1.50	1.56	1.64
CaO	0.62	0.54	-	0.20	0.09	-
Na_2O	1.27	1.33	1.54	0.89	0.93	1.08
K_2O	3.53	3.69	4.31	3.47	3.62	4.23
P_2O_5	0.08	-	-	0.09	-	-
H_2O	2.77	-	-	2.89	-	-
	99.67	100.00	100.00	99.79	100.00	100.00

Table 3

Grain	1	2	3	4	5	6	7	8	9	10	11	13	15	16	17	18	19	20	21
	mtx	in St	mtx	in St	mtx	mtx	mtx	mtx	in Grt	in Grt	mtx	mtx	in Grt	in Grt	in Grt	mtx	mtx	in Tur	in Tur
SiO_2	0.43	0.31	0.26	0.40	0.33	0.57	0.40	0.32	0.34	0.70	0.35	0.40	0.48	0.57	0.89	0.62	0.55	0.41	0.36
P_2O_5	29.2	30.1	29.8	29.7	27.8	30.1	29.6	29.9	29.4	31.1	28.8	30.0	28.9	31.1	28.9	28.5	28.7	25.3	26.1
SO_3	0.03	0.01	0.01	0.03	0.03	0.02	0.03	0.03	0.03	0.03	0.02	0.03	0.04	0.03	0.06	0.03	0.04	0.02	0.03
CaO	0.81	0.59	1.00	0.60	1.00	0.98	0.97	0.46	0.72	0.63	1.01	1.17	0.64	0.68	0.82	0.93	1.20	0.79	0.70
Y_2O_3	0.15	0.11	0.09	0.15	0.07	0.30	0.35	0.09	0.03	0.00	0.16	0.29	0.02	0.05	0.02	0.07	0.09	0.09	0.13
La_2O_3	15.1	15.0	15.0	15.4	14.9	14.4	14.8	15.1	15.2	15.3	14.6	14.3	15.6	15.2	15.1	14.4	14.1	14.7	15.3
Ce_2O_3	30.0	31.2	30.2	30.8	30.0	28.6	29.7	31.1	30.9	31.2	29.6	29.1	30.5	27.6	29.8	29.4	28.6	29.7	29.6
Pr_2O_3	3.23	3.40	3.21	3.35	3.23	3.13	3.20	3.34	3.33	3.46	3.24	3.18	3.28	2.94	3.21	3.19	3.10	3.21	3.15
Nd_2O_3	12.0	12.2	11.7	12.2	11.7	11.7	11.7	12.4	12.1	12.1	11.9	11.6	12.1	11.6	12.0	11.7	11.3	11.7	11.9
Sm_2O_3	1.96	1.98	1.91	2.06	1.84	2.00	1.99	2.06	1.95	1.90	2.07	1.93	1.93	1.96	1.96	1.91	1.83	1.89	1.97
Gd_2O_3	1.13	0.89	0.88	0.99	0.80	1.23	1.13	0.91	0.79	0.67	1.13	1.08	0.69	0.83	0.75	0.83	0.83	0.90	0.97
Dy_2O_3	0.14	0.11	0.11	0.14	0.10	0.24	0.26	0.09	0.09	0.06	0.16	0.17	0.05	0.07	0.07	0.10	0.10	0.13	0.11
PbO	0.088	0.071	0.119	0.085	0.098	0.118	0.110	0.067	0.086	0.071	0.092	0.116	0.080	0.098	0.099	0.107	0.127	0.098	0.087
ThO_2	4.69	3.07	4.83	3.13	4.23	6.25	5.17	2.31	3.79	3.26	4.65	4.95	3.45	3.51	4.16	5.17	5.71	4.07	3.35
UO_2	0.55	0.39	0.99	0.62	0.69	0.54	0.68	0.50	0.53	0.48	0.59	0.89	0.44	0.63	0.56	0.56	0.73	0.55	0.57
Sum	99.68	99.58	100.24	100.21	97.56	100.34	100.25	99.09	99.37	101.62	99.34	100.06	99.81	97.48	99.99	97.82	97.86	93.58	94.34
Si	0.017	0.012	0.010	0.016	0.013	0.022	0.016	0.012	0.013	0.027	0.014	0.015	0.019	0.022	0.034	0.025	0.022	0.018	0.015
P	0.979	0.997	0.989	0.981	0.957	0.990	0.982	0.994	0.986	0.994	0.965	0.982	0.956	1.017	0.949	0.972	0.969	0.931	0.942
S	0.001	0.000	0.000	0.001	0.001	0.001	0.001	0.001	0.001	0.001	0.001	0.001	0.001	0.001	0.002	0.001	0.001	0.001	0.001
Ca	0.035	0.025	0.042	0.025	0.044	0.041	0.041	0.019	0.031	0.026	0.043	0.048	0.027	0.028	0.034	0.040	0.051	0.036	0.032
Y	0.003	0.002	0.002	0.003	0.001	0.006	0.007	0.002	0.001	0.000	0.003	0.006	0.000	0.001	0.001	0.002	0.002	0.002	0.003
La	0.221	0.217	0.216	0.221	0.224	0.207	0.214	0.219	0.222	0.213	0.213	0.204	0.224	0.217	0.216	0.214	0.207	0.235	0.240
Ce	0.435	0.447	0.434	0.439	0.446	0.407	0.426	0.447	0.448	0.431	0.428	0.411	0.436	0.389	0.422	0.433	0.417	0.473	0.462
Pr	0.047	0.049	0.046	0.048	0.048	0.044	0.046	0.048	0.048	0.048	0.047	0.045	0.047	0.041	0.045	0.047	0.045	0.051	0.048
Nd	0.171	0.171	0.164	0.170	0.170	0.163	0.164	0.174	0.171	0.164	0.168	0.160	0.169	0.159	0.166	0.168	0.160	0.181	0.181
Sm	0.027	0.027	0.026	0.028	0.026	0.027	0.027	0.028	0.027	0.025	0.028	0.026	0.026	0.026	0.026	0.027	0.025	0.028	0.029
Gd	0.015	0.012	0.011	0.013	0.011	0.016	0.015	0.012	0.010	0.008	0.015	0.014	0.009	0.011	0.010	0.011	0.011	0.013	0.013
Dy	0.002	0.001	0.001	0.002	0.001	0.003	0.003	0.001	0.001	0.001	0.002	0.002	0.001	0.001	0.001	0.001	0.001	0.001	0.001
Pb	0.0009	0.0008	0.0013	0.0009	0.0011	0.0012	0.0012	0.0007	0.0009	0.0007	0.0010	0.0012	0.0008	0.0010	0.0010	0.0012	0.0014	0.0012	0.0011
Th	0.042	0.027	0.043	0.028	0.039	0.055	0.046	0.021	0.034	0.028	0.042	0.044	0.031	0.031	0.037	0.047	0.052	0.040	0.032
U	0.005	0.003	0.009	0.005	0.006	0.005	0.006	0.004	0.005	0.004	0.005	0.008	0.004	0.005	0.005	0.005	0.007	0.005	0.005
Age(Ma)	322	389	349	393	359	347	351	402	370	347	330	349	388	418	392	363	371	395	396
1σ	19.0	28.0	16.2	24.4	19.5	16.4	17.4	30.9	22.5	24.4	18.6	16.6	24.4	23.6	21.1	18.3	16.8	21.1	23.8

Figure S1

Figure S2

Click here to access/download
Supplementary material/Appendix (Files for online publication only)
Fig. S2.tif

Figure S3

Click here to access/download
Supplementary material/Appendix (Files for online publication only)
Fig. S3.tif

Figure S4

Figure S5

Click here to access/download
Supplementary material/Appendix (Files for online publication only)
Fig. S5.tif

Table S1

Click here to access/download
Supplementary material/Appendix (Files for online publication only)
Table S1.xlsx